Received: 25 May 2023 | Revised: 23 October 2023 | Accepted: 22 November 2023

DOI: 10.1002/joc.8324

RESEARCH ARTICLE

International Journal of Climatology RMetS

Aerosol characteristics in CMIP6 models' global simulations and their evaluation with the satellite measurements

Jaisankar Bharath[1,2] | Tumuluru Venkata Lakshmi Kumar[1,2,6] | Vanda Salgueiro[3,4] | Maria João Costa[3,4] | Rajesh Kumar Mall[5]

[1]Centre for Atmospheric Sciences and Climate Studies, SRM Institute of Science and Technology, Kattankulathur, India

[2]Department of Physics and Nanotechnology, SRM Institute of Science and Technology, Kattankulathur, India

[3]Earth Remote Sensing Laboratory (EaRSLab), University of Évora, Évora, Portugal

[4]Institute of Earth Sciences (ICT) and Department of Physics, University of Évora, Évora, Portugal

[5]DST-Mahamana Center of Excellence in Climate Change Research, Institute of Environment and Sustainable Development, Banaras Hindu University, Varanasi, India

[6]School of Environmental Sciences, Jawaharlal Nehru University, New Delhi, India

Correspondence
Tumuluru Venkata Lakshmi Kumar, Centre for Atmospheric Sciences and Climate Studies, SRM Institute of Science and Technology, Kattankulathur 603203, Tamilnadu, India.
Email: lkumarap@hotmail.com

Funding information
National Portugese Funds, Grant/Award Numbers: UIDB/04683/2020, UIDP/04683/2020

Abstract

Global and regional trends of the Aerosol Optical Depth (AOD) from Coupled Model Intercomparison Project (CMIP) Phase 6 simulations for the study period 1971–2014 were compared against the satellite retrievals and the inter-model variations were analysed. The AOD from multimodel mean (MMM) of eight general circulation models (GCMs) has been evaluated against the Moderate Resolution Imaging Spectroradiometer (MODIS) and Multi-angle Imaging Spectro Radiometer (MISR) AOD for the 2001–2014 period. Angstrom exponents (AE and its first derivative) that represent the size distribution of aerosols are estimated globally from the perturbed initial condition ensemble of MRI-ESM2-0 and MPI-ESM-1-2-HAM models to report the aerosol variations through their size distribution. We found that the global AOD obtained from the MMM8 showed an insignificant decreasing trend, while this trend is significantly positive over the northern tropical region. The MMM8 has overestimated the MODIS AOD over North Africa, India, China, and Australia while this overestimation is confined to North Africa and eastern China when compared against MISR AOD. The absolute percent bias of MMM8 is 28.1% and 24.1% over the globe when compared against MODIS and MISR AOD, respectively. The spatial pattern of AE showed the dominance of fine- and coarse-mode particles during the boreal/austral winter and summer seasons, respectively, that replicate the seasonality of aerosols. The AE derived from MPI-ESM-1-2-HR demonstrated better agreement with AATSR SU's (Advanced Along Track Scanning Radiometer instrument series, with the algorithm developed by Swansea University) AE (550–870 nm). On the other hand, MRI-ESM2-0 consistently underestimated AE across different regions and wavelength ranges, suggesting an over representation of larger aerosol particles in the model's portrayal of aerosol size distribution compared to satellite observations.

KEYWORDS

Aerosol Optical Depth, Angstrom exponent, CMIP6, MISR, MODIS

1 | INTRODUCTION

Atmospheric aerosols (AA), one of the important climate-forcing agents, imply a significant impact on the changing climate. AA perturb the atmosphere directly by the extinction of incoming solar radiation (Andreae et al., 2005; Jung et al., 2019) and indirectly by altering the cloud properties (Christensen et al., 2020; Ramanathan et al., 2001). Besides, AA can influence human health by causing respiratory and cardiovascular diseases depending on their size, type, and composition (Lelieveld et al., 2013). The increasing (decreasing) trend of aerosol emissions in the atmosphere causes a decline (increase) in the solar radiation received at the surface, which is termed as the dimming (brightening) effect (Wild et al., 2005). Since the late 1980s, the increasing trend of AA has been reversed to a decreasing trend over the Northern Hemisphere, causing an increment in incoming shortwave solar radiation at the Earth's surface (Quaas et al., 2022; Wild, 2010; Wild et al., 2005). This dimming-to-brightening effect can potentially strengthen the warming trend caused due to greenhouse gases and significantly influence the earth's hydrological cycle.

As a result of air pollution reduction policies executed in several regions such as Europe and Northern America from the 1970s, anthropogenic aerosol emissions have decreased (Wild, 2010). In contrast, air pollution due to the utilization and use of fossil fuels has expanded unequivocally in other regions. Particularly, Southeast Asia and Africa have had a general increment in AA since the mid-1970s (Klimont et al., 2013; Smith & Bond, 2014; Stohl et al., 2015). In contrast, Europe and Northern America showed a decrement in aerosol loading since the mid-1980s (Wild et al., 2005). From the satellite observations, it is evident that the spatiotemporal distribution of AA over Asia has changed (Myhre et al., 2013; Ramachandran et al., 2020) mainly due to the increase in the anthropogenic emissions of aerosols and their precursors (Ramachandran et al., 2020; Samset et al., 2019).

Hence, it is important to have a precise representation of the long-term global and regional aerosol burden for a better understanding of their role in the climate. General circulation models (GCMs) simulate and provide the AA concentration in the atmospheric column by considering both natural and anthropogenic sources. The ability of GCMs to accurately simulate the atmosphere in the historical period is a matter of great concern to rely upon future projections. In the present work, we focused on the historical simulations of aerosol optical depth (AOD), a measure of radiation extinction, used as a proxy for aerosol concentration from GCMs' simulations. New generation models such as ECHAM6-HAM2, EMEP/MSC-W, GISS, NorESM1, OsloCTM2, and SPRINTARS which participated in the European Union project ECLIPSE, used identical and improved anthropogenic emission data for the 1990–2015 period from ECLIPSE to simulate the AOD (Klimont et al., 2017; Stohl et al., 2015). Myhre et al. (2017) studied the multimodel mean of the above-said models and reported that the models have reproduced the large-scale changes in surface aerosol over the United States and Europe.

Coupled Model Intercomparison Project (CMIP) is the result of a coordinated effort of climate modellers across the globe that provided distinct and updated simulated datasets of new-generation GCMs. The CMIP6 models use biogeochemical processes of aerosols represented in earth system models for the simulation of climate and atmosphere. The future projection pathways of CMIP6 are known as shared socioeconomic pathways (SSPs). Unlike the representative concentration pathways (RCP) of the CMIP5, the 6th phase SSPs incorporated additional attributes such as land, energy use, and economic activities along with the impact of emissions for respective scenarios (Eyring et al., 2016). Aerosol optical depth from CMIP GCMs had been used to understand the relationship of AA with the global water cycle (Boé, 2016; Lin et al., 2018; Monerie et al., 2022; Sanap et al., 2015; Sobel et al., 2019), their influence on clouds (Cherian & Johannes, 2020; Frey et al., 2017; Hua et al., 2020; Luo et al., 2021) and Asian aerosol dipole patterns (Ramachandran et al., 2022; Wang et al., 2021). Spatiotemporal variations of AA in CMIP5 and CMIP6 models in eastern central China report an underestimation of AOD that decreased from 40% (CMIP5) to 8% (CMIP6) in comparison with satellite AOD during 2000–2005 (Ali et al., 2022; Li et al., 2021).

It was also reported that the CMIP phase 5 models have not precisely depicted the fundamental cloud processes (Lauer & Hamilton, 2013) and due to this, the CMIP5 model's simulated aerosol-cloud interactions are not reliable, causing errors in the radiative forcing values. Furthermore, Sanap et al. (2014) reported an anomalous easterly wind bias in most of the CMIP5 models resulting in a disagreement in simulated dust aerosols when compared against the satellite retrievals for the 2001–2005 period over the South Asian region. The updated CMIP6 GCMs with more exhaustive aerosol–cloud interactions simulate the general circulation features in a better way (Chung & Soden, 2017; Ekman, 2014). So, it is exceptionally intriguing to see how these new-generation models simulate the latitudinal trends and spatiotemporal size distribution of aerosols globally. With the increasing number of GCMs' simulations of AOD, a clear picture of the evaluation of AOD datasets are of prime importance. Cherian and Johannes (2020) carried out the spatial trend analysis of AOD and cloud parameters from seven CMIP5 and five CMIP6 models (CanESM5, GFDL-CM4,

TABLE 1 List of CMIP6 models along with resolution and data availability used in this study (https://esgf-node.llnl.gov/search/cmip6/)

Model	Modelling centre	Model resolution	AOD availability (λ)		
			550 nm	440 nm	870 nm
ACCESS-CM2	CSIRO, Australian Research Council Centre of Excellence for Climate System Science (ACCESS), Australia	1.875° × 1.25°	✓	✓	✗
AWI-ESM-1-1-LR	Alfred Wegener Institute (AWI), Germany	1.875° × 1.875°	✓	✗	✗
BCC-ESM1	BCC, China	2.813° × 2.813°	✓	✗	✗
CESM2	NCAR, USA	1.25° × 0.93°	✓	✗	✗
CESM2-FV2	NCAR, USA	2.5° × 1.875°	✓	✗	✗
CESM2-WACCM	NCAR, USA	1.25° × 0.938°	✓	✗	✗
CESM2-WACCM-FV2	NCAR, USA	2.5° × 1.875°	✓	✗	✗
CMCC-CM2-SR5	CMCC, Italy	1.25° × 0.938°	✓	✗	✗
CMCC-ESM2	CMCC, Italy	1° × 1°	✓	✗	✗
E3SM-1-0	E3SM-Project, LLNL	1° × 1°	✓	✗	✗
E3SM-1-1	E3SM-Project, RUBISCO	1° × 1°	✓	✗	✗
E3SM-1-1-ECA	E3SM-Project	1° × 1°	✓	✗	✗
GFDL-CM4	NOAA GFDL, USA	1.25° × 1°	✓	✗	✗
GFDL-ESM4	NOAA GFDL, USA	1.25° × 1°	✓	✓	✓
INM-CM4-8	INM, Russia	2° × 1.5°	✓	✗	✗
INM-CM5-0	INM, Russia	2° × 1.5°	✓	✗	✗
IPSL-CM6A-LR	IPSL, France	2.5° × 1.259°	✓	✓	✓
IPSL-CM6A-LR-INCA	IPSL, France	2.5° × 1.259°	✓	✓	✓
KACE-1-0-G	National Institute of Meteorological Sciences/Korea Meteorological Administration (NIMS-KMA), Republic of Korea	1.875° × 1.875°	✓	✗	✗
MIROC6	MIROC, Japan	1.405° × 1.406°	✓	✗	✓
MPI-ESM-1-2-HAM	HAMMOZ-Consortium	1.875° × 1.875°	✓	✓	✓
MPI-ESM1-2-HR	MPI-M, DWD, DKRZ	0.938° × 0.937°	✓	✗	✗
MPI-ESM-1-2-LR	MPI-M, AWI	1.875° × 1.875°	✓	✗	✗
MRI-ESM2-0	MRI, Japan	1.125° × 1.125°	✓	✓	✓
NorESM2-LM	NCC, Norway	2.5° × 1.875°	✓	✗	✗
NorESM2-MM	NCC, Norway	1.25° × 0.938°	✓	✓	✓

IPSL-CM6A-LR, HadGEM3-GC31-L and MIROC-ES2L) simulations in aerosol source regions to understand the link between emission trends and cloud radiative effects and the results were compared with the MODIS retrievals. Mortier et al. (2020) conducted a comparative analysis of aerosol products from AeroCom Phase III models and four CMIP6 models (NorESM2, CanESM5, CESM2, IPSL-CM6A) against ground observations from AERONET.

The present work performs the analysis based on the eight CMIP6 simulations that have been selected from 26 available CMIP6 models by applying the statistical performance metrics. Further, we have used the ensemble of eight models' AOD (Table 1), which are different from the previous studies, to compare against the AOD of MODIS and MISR on a global scale. In the second part of the work the AE derived from the models have been compared against the same obtained from the MODIS and AATSR SU. The results of the present study will fulfil the gap of the earlier studies by discussing the model AOD and AE variations globally with reference to multiple satellite retrievals.

The main objectives of the present work are as follows:

1. To analyse the spatiotemporal variations of AOD simulations from individual GCMs and their multimodel mean (MMM) over different latitudinal belts and aerosol source regions of the globe for the period of 1971–2014.
2. Comparison of the simulated AOD of MMM with the satellite (MODIS and MISR) derived AOD for the period 2001–2014 to report the biases in the model AOD.
3. To obtain the Angstrom exponents (AE), using two and three wavelength dependence AODs, for understanding the aerosols' size distribution over the globe for the period 1971 to 2014, and comparison with the AE calculated from the satellite retrievals (MODIS and AATSR SU).

2 | DATA AND METHODOLOGY

Historical simulations of monthly mean AOD from the 26 GCMs of the CMIP6 (Eyring et al., 2016) for the period of 1971–2014 have been utilized in this study. Details of the models used in this study are listed in Table 1. The analysis is carried out by using the simulated datasets under the variant label "r1i1p1f1" and "historical" experiment which is forced by the observation-based external forcings (Eyring et al., 2016). The datasets can be accessed from https://esgf-node.llnl.gov/.

The AOD retrievals from Moderate Resolution Imaging Spectroradiometer (MODIS) and Multi-angle Imaging SpectroRadiometer (MISR) from the Goddard Earth Sciences Data and Information Services Center (GES DISC, NASA) have been used in the present work. The availability of the MODIS and MISR AOD are from February 2000 and March 2000 onwards, respectively. The level 3 monthly data of AOD at mid-visible wavelength (550 nm) retrievals of MODIS (combined Terra and Aqua) from the merged product from the Dark Target and Deep Blue combined algorithm were used in the present work. The accuracy of MODIS AOD is expected to be within the $\pm$ [0.05 + (0.15 $\times$ AOD)] error envelope (Kaufman et al., 1997; Levy et al., 2013). The MISR measures the atmospheric and surface properties using multiple viewing angles. The level 3 AOD at 555 nm data in a grid of $0.5^\circ \times 0.5^\circ$ resolution was used considering that the small difference in the reference wavelength does not introduce considerable errors. This approximation is considered in multiple previous studies (Deep et al., 2021; Kang et al., 2016; Zhao et al., 2018). The MISR AOD can have uncertainties up to $\pm 0.20 \times$ AOD (Kahn et al., 2001; Kahn et al., 2010).

Reanalysis data sets of wind at 850 hPa have been obtained from the National Centre for Environmental Prediction (NCEP) with $2.5^\circ \times 2.5^\circ$ resolution for the period 1971–2014. The data is available on a monthly scale and can be obtained from https://psl.noaa.gov/data/gridded/data.ncep.reanalysis.html. The wind data at 850 hPa is found to be the better indicator of weather patterns over large areas (Neal et al., 2020) and the altitude equivalent to 850 hPa is sufficiently distant from the surface topography and represents the well-mixed atmosphere. All the datasets were brought into a common resolution of $1^\circ \times 1^\circ$ by using the bilinear interpolation method since the individual model and satellite data have various space-scale resolutions.

Our aim in the present work is to study the model AOD trends and the models' ability in simulating the reference AOD, that is, MODIS and MISR. An MMM is to be obtained from the individual models which minimizes the uncertainties. However, the selection of models for obtaining the MMM is very much required since all the models do not have agreement either with the magnitude or with the pattern as reference AOD datasets show. In the present study, the selection of models has been done by examining each model's performance against the combined satellite (MODIS and MISR) mean annual AOD data for the 2001–2014 period. Since the satellite AOD data is available from the year 2000 onwards for MODIS and MISR which is shorter compared to the modelled data period, we have also evaluated the individual models against the MMM of all 26 GCMs (MMM26) for the 1971–2014 period (Misra et al., 2016; Pu & Ginoux, 2018).

The Taylor diagram (Figure 1a,b) shows the correlations of AODs obtained from each GCMs, averaged over the globe with the reference mean annual AOD data along with the normalized standard deviations. From Figure 1, it is possible to decipher the extent of agreement of individual models with the reference data, from these eight models, namely AWI-ESM-1-1-LR, BCC-ESM-1, CESM2-WACCM, CESM2-WACCM-FV2, MPI-ESM-1-2-HR, MPI-ESM-1-2-HAM, MPI-ESM-1-2-LR and MRI-ESM2-0, which have the significant correlation of 0.9+ with MMM26 for the period 1971–2014 (Figure 1a) and the same all models have a correlation of +0.6 and above (expect MRI-ESM-0 which have $r = +0.51$) with satellite data (Figure 1b). From these eight models, MMM8 was obtained and proceeded in the study. The normalized standard deviation of MMM8 is high ($\sim$3.18) when compared with MMM26, which might be due to the reason that the variability amplitude of MMM26 has been washed out by the inclusion of many models with lower AOD. Also, the MMM8 has the highest correlation ($r = 0.7$) and a normalized standard deviation of 0.78 with

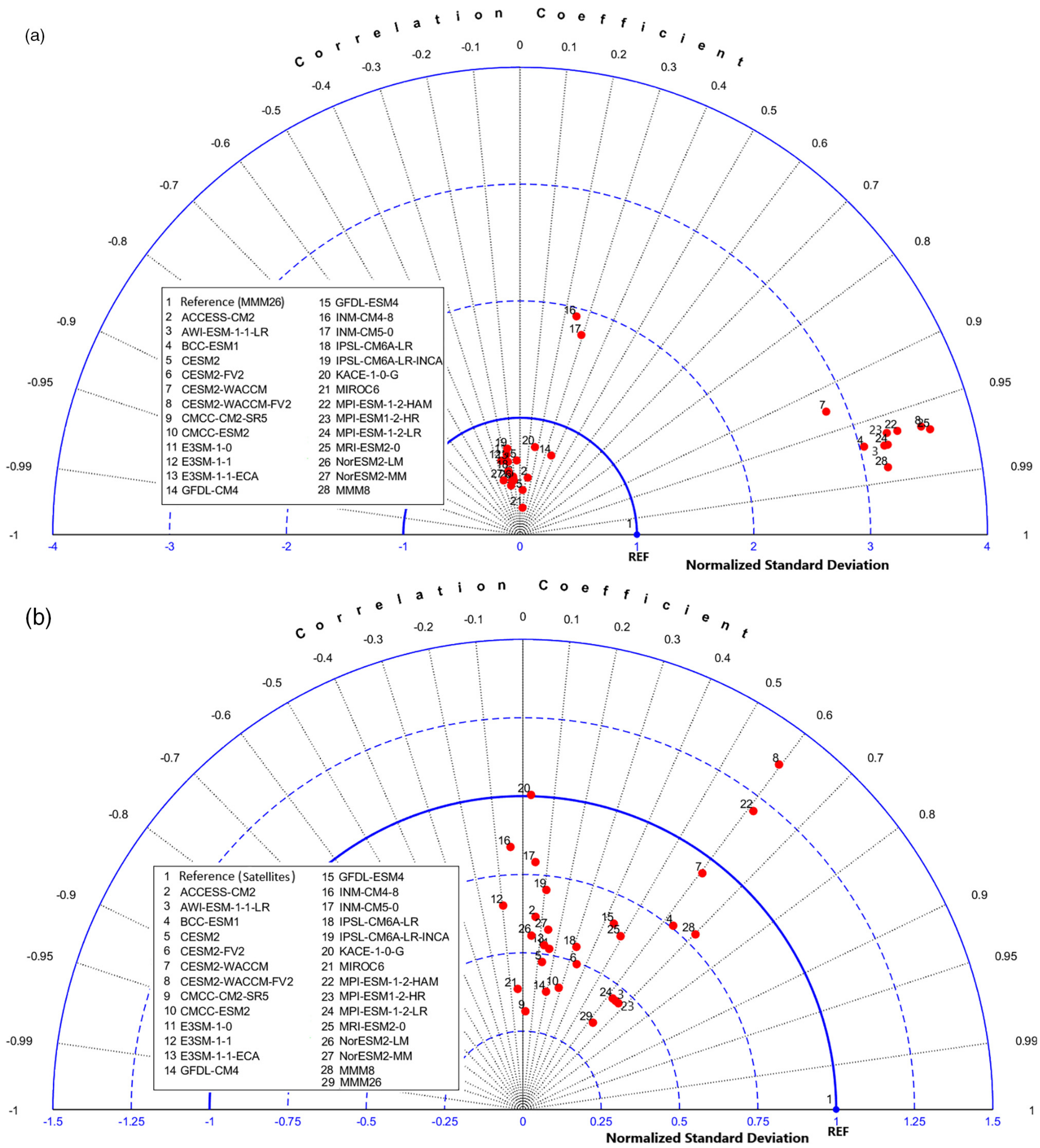

FIGURE 1 Taylor diagrams showing the correlation coefficients and normalized standard deviation of mean annual AOD for individual 26 GCMs and MMM against the reference AOD (a) MMM of 26 GCMs (MMM26) and (b) combined satellite AOD (MODIS and MISR) [Colour figure can be viewed at wileyonlinelibrary.com]

the satellite data. Please note that we have used the MMM of the GCMs with similar climate initial conditions, that is, with the single realizations, in the present study and this MMM approach itself is a way of minimizing the internal uncertainty or bias compared to other individual models (Hawkins & Sutton, 2009). The use of MMM will help us to evaluate how well the climate system is simulated by the GCMs (Tebaldi and Knutti, 2007).

We have also verified the spatiotemporal pattern of the mean annual AOD of individual 26 GCMs, MMM8, MMM26, and satellite retrievals (MODIS and MISR) for the 2001–2014 period (Figures S1 and S2a–o, Supporting Information). From the figures, it is observed that the models such as INM-CM5-0 and INM-CM4-8 could not capture the tropical mean AOD when compared with MODIS and MISR AOD features. The models such as MIROC6, CMCC-ESM2, and CMCC-CM2-SR5 could not show the spatial pattern of mean AOD across the globe as shown by the satellites. The inclusion of these models in obtaining the MMM affects the spatiotemporal compatibility of the model simulated AOD with the satellite datasets. Hence, the method followed in the present study to obtain the MMM of eight selected models is a better choice since its large-scale features of AOD are comparable with the reference datasets.

The latitudinal trends of AOD for the period 1971–2014 were calculated for individual eight CMIP6 GCMs that have been used for MMM8. The trend analysis was carried out using the least square linear trend method for the Globe, Northern and Southern Hemispheres, Tropics, middle latitudes and polar regions of both hemispheres. The following abbreviations are used to represent the regions (the latitudinal ranges have been provided in the parenthesis): NP, northern polar region (61°–90°N); NM, northern midlatitude region (31°–60°N); NT, northern tropical region (0°–30°N); ST, southern tropical region (0°–30°S); SM, southern midlatitude region (31°–60°S); SP, southern polar region (61°–90°S); NH, Northern Hemisphere (0°S–90°N); SH, Southern Hemisphere (0°N–90°S). This regression method used in the present work for the trend analysis is a straightforward and robust technique that is widely adopted to assess the time-dependent geological and ecological variables trends and it is less sensitive to the discontinuance in the time series of data. The method is very suitable for data having constant uncertainty, that is, Gaussian white noise (Ramachandran et al., 2020). The two-tailed Student *t*-test was applied to compute the statistical significance of the latitudinal trend. In the present study, the trend analysis has been carried out for the period 1971–2014 by taking the mean annual AOD on the *Y*-axis and the years on the *X*-axis. The slope of the linear fit between any two points on the fit trend line is considered as the trend value. The trend analysis has been carried out separately for the land, ocean, and combined regions (land–ocean together).

We analysed the mean AOD from CMIP6 GCMs with MODIS and MISR satellite data by estimating the percent bias for the period 2001–2014. The percent bias has been obtained by taking the percentage ratio of the difference in mean annual AOD between the model and satellite to the satellite AOD, and the average percent bias of the spatial pattern of AOD for the study period. Since the sign of bias can change its magnitude when averaged over a large area, we have also calculated the absolute bias of MMM8 with MODIS and MISR AOD for the different latitudinal belts as well as for the regions of United States, Europe, India, and China where the significant trends of aerosols took place. As the MODIS data is available from 2001 onwards for all months, we could use model data from 2001 to 2014 for comparison purposes. Though MODIS and MISR give updated AOD data for the current year also, the historical simulations of CMIP6 end by 2014.

The Angstrom exponent (AE) and its first derivative were calculated from the AOD simulation datasets for the period 1971–2014. The AE and its first derivative provide information on the size distribution of aerosols. The AE (α) can be calculated using the wavelength dependence AODs (τ) at a minimum of two different wavelengths (λ_1, λ_2). For obtaining the AE, the combination of AOD at 440 and 550, 550 and 870, and 440 and 870 nm were used from the perturbed initial condition ensemble for two models, MRI-ESM2-0 and MPI-ESM-1-2-HAM. It should be noted that the other models that were used for MMM8 do not have AOD at 440 and 870 nm wavelengths. Hence, we have used the aforementioned models only, to estimate the AE and its first derivative. We have adopted the perturbed initial condition ensemble approach when estimating the AE from these two individual GCMs. Based on the availability, we have used ten realizations for MRI-ESM2-0 and three realizations for MPI-ESM-1-0-HAM in the present study to estimate the spatial pattern of AOD.

The first derivative of AE was obtained using the AODs at 440, 550, and 870 nm from the above-mentioned models. The formulae for calculating the AE (Equation (1)) and the derivative of AE (Equation (2)) (Eck et al., 2001; Knobelspiesse et al., 2004) are presented below,

$$\alpha = -\frac{d\ln\tau}{d\ln\lambda} = -\frac{\ln\left(\frac{\tau_1}{\tau_2}\right)}{\ln\left(\frac{\lambda_1}{\lambda_2}\right)}, \tag{1}$$

$$\alpha'(\lambda_i) = \frac{d\alpha}{d\ln\lambda} = -\left(\frac{2}{\ln\lambda_{i+1} - \ln\lambda_{i-1}}\right)\cdot \left(\frac{\ln\tau_{i+1} - \ln\tau_i}{\ln\lambda_{i+1} - \ln\lambda_i} - \frac{\ln\tau_i - \ln\tau_{i-1}}{\ln\lambda_i - \ln\lambda_{i-1}}\right). \tag{2}$$

The analysis of spatial variations of AE and its first derivative provides inferences on the dominance of fine- and coarse-mode particles across different regions. The AE was studied for the January and July months, which represent the winter and summer season months in the Northern Hemisphere and vice versa in the Southern Hemisphere. Additionally, in the regional aspect of the tropical monsoon regions, January/July are non-monsoon/monsoon months of the year. This allows a clear distinction of seasonality in aerosols in which their size matters predominantly.

To verify the Angstrom exponent (AE) acquired through the perturbed parameter ensembles (PPE) of both models, we employed data from MODIS and AATSR SU v4.3 (Advanced Along Track Scanning Radiometer instrument series, with the algorithm developed by Swansea University). MODIS provides AOD values across three spectral

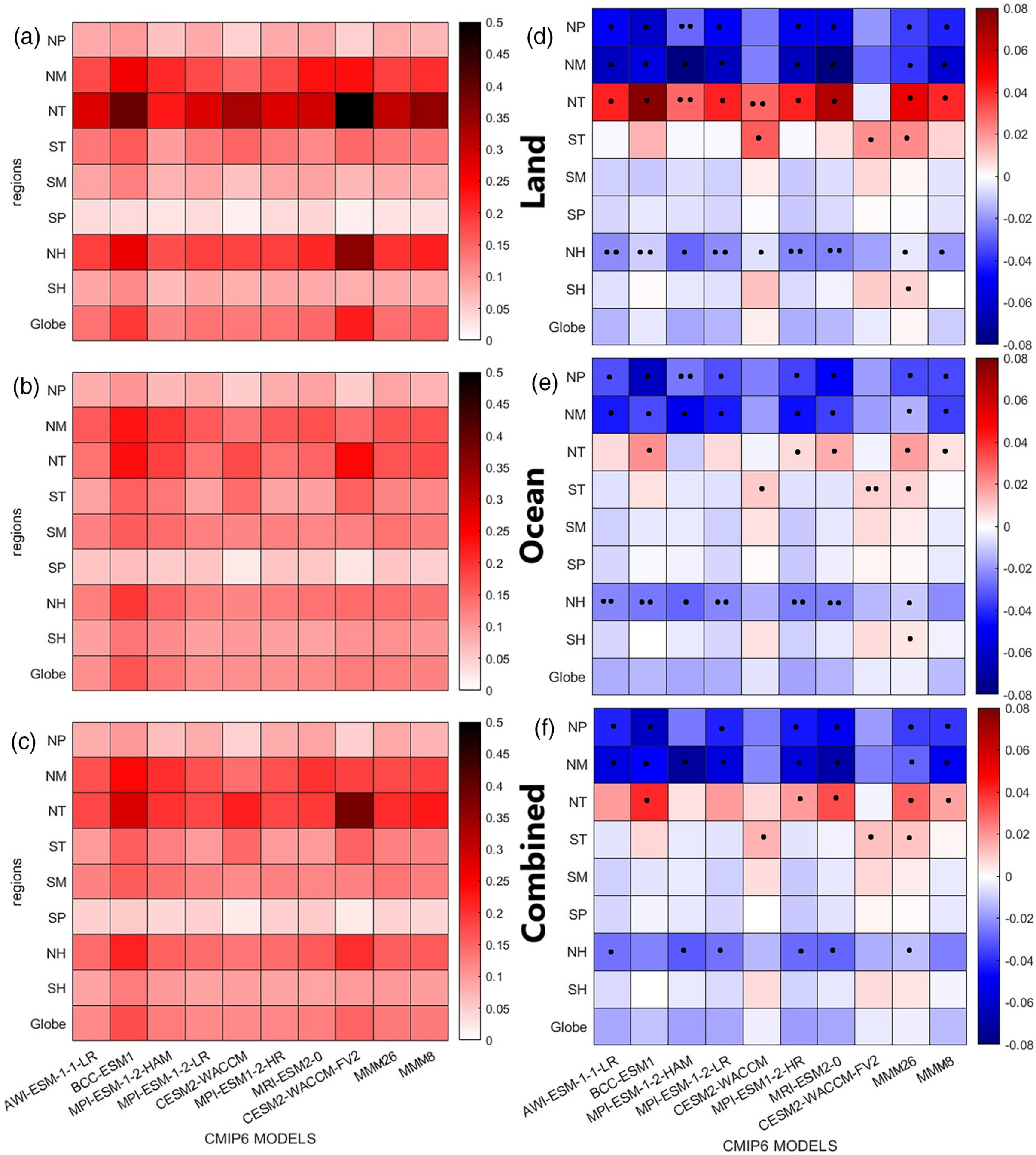

FIGURE 2 Heat maps of mean annual AOD at 550 nm (a–c) and the trend values of mean annual AOD at 550 nm (d–f) for the period of 1971–2014 were obtained from the eight selected individual models along with MMM8 for land (a, d), ocean (b, e) and combined regions (c, f) over tropical, mid-latitudinal and polar regions of Southern and Northern Hemispheres, Southern and Northern Hemispheres as the whole and the entire globe. Single dots in the boxes denote the statistical significance of the trend at 0.01 level, double dot denotes the same but at 0.05 level [Colour figure can be viewed at wileyonlinelibrary.com]

bands (470, 550, and 660 nm) over land. To enable a meaningful comparison with the model's AOD (440 nm), we standardized the MODIS AOD at 470 nm by interpolating it to a 440 nm wavelength using a wavelength-dependent AOD-to-AE relation as in Equation (1), a similar interpolation method has been used in many recent studies (Mukkavilli et al., 2019; Qi et al., 2013). Specifically, we used the AE values within the 410–470 nm range from MODIS for this purpose. Following the interpolation, the AOD at 440–550 nm was employed to calculate AE using the same equation. It is worth noting that this study utilized level 3 output data, provided at both daily and monthly resolutions, with a 1° × 1° spatial resolution, designed for climate model comparisons. In the case of AATSR SU, the AOD data corresponding to the common wavelength spectra of 550 and 870 nm for the 2002–2012 period is available. Consequently, we utilized these wavelengths to compute AE. However, the studies on the evaluation of AOD using AATSR SU are very few, and evaluation studies on AATSR SU against ground-based reference data are limited, accordingly, the AOD of MODIS and MISR were only utilized for the selection of models to obtain the MMM in this study.

3 | RESULTS AND DISCUSSION

3.1 | Spatiotemporal variations of AOD simulations and their trends

The mean annual AOD for the global and latitudinal bands along with the trends over the land, ocean, and the combined regions are depicted in Figure 2a–c,d–f for the study period 1971–2014. The dots in different boxes of Figure 2d–f denote the statistical significance of AOD trends in those respective latitudinal bands. Single and double dots represent the 0.01 and 0.05 levels of significance, respectively. To enable a meaningful comparison of these values with satellite retrievals, we present the mean and trend values of the models' Aerosol Optical Depth (AOD) for the period spanning from 2001 to 2014, along with MISR and MODIS AOD, in Figure S3. Given the relatively shorter study period when satellite observations are included, the trend values and levels of statistical significance vary between Figures 2 and S3. Among the eight GCMs, CESM-WACCM-FV2 showed the highest value of AOD over the NT over the land (>0.7), ocean (>0.25), and combined region (>0.3) during the study period when compared to the other GCMs (Figure 2a–c). As reported by Zhao et al. (2022), this high value of AOD over the NT is due to the higher values of dust aerosols simulated by the model CESM-WACCM-FV2 over the desert regions of Northern Africa and the Middle East which was also pronounced in our analysis (Figure S1k). Similarly, the lower values of AOD are shown by the same model CESM-WACCM-FV2 over land (∼0.005), ocean (∼0.02), and combined regions (∼0.01) of the SP region (Figure 2a–c). From the visual inspection, it can be observed that the mean AOD variability is high over the land compared to the ocean and combined regions, which is evidenced by the standard deviations of ∼0.03, 0.02, and 0.025, respectively. All the models along with the MMM8 showed higher values in the Northern Hemisphere tropical region. AWI-ESM-1-1-LR, BCC-ESM-1-2, MPI-ESM-1-2-HAM, MPI-ESM-1-2-HR, MPI-ESM-1-2-LR, and MRI-ESM-2-0 models have shown significant negative trends over NM, NP over the land, ocean, and combined regions. During the 2001–2014 period, all the models kept a similar mean AOD and trend pattern with minor changes in the magnitude, when compared these satellite AOD MODIS depicts a significant positive trend in the NT similar to the models, whereas MISR also shows a positive trend in NT in land and combined regions but the values were statistically insignificant (Figure S3). While in the NM regions, the MODIS and MISR showed an insignificant increasing trend of AOD, on the other hand, MISR and models showed a decreasing trend pattern. This dissimilarity between models and satellite products is discussed further while discussing the model biases in the next subsection. CESM2-WACCM model showed positive significant trends over ST, SH in the land region and ST in the oceanic and combined regions (Figure 2). The model MRI-ESM-2-0 showed negative trends in NM, NP in oceanic regions and NH in the combined regions while the model CESM2-WACCM showed a significant positive trend over ST in the land region. The mixed trends of AOD in all these models infer the intermodel variability and discrepancy among the models. As illustrated in Figures 3a, S1, and S2, the mean AOD value in the Southern Hemisphere (ST) appears lower when contrasted with the Northern Hemispheric regions. While the majority of the models exhibit an insignificant trend in the ST region, both the models and satellite data from CESM2-WACCM and CESM2-WACCM-FV2 reveal a significant positive trend. This arises from the fact that the model has a tendency to overestimate the presence of dust aerosols and simulate a more pronounced southward transport of these dust particles in comparison to observational data (Zhao et al., 2022). The MMM8 showed significant decreasing trends over the Northern Hemispheric belts whereas these trends are insignificant without trend in the Southern Hemispheric regions (Figure 2d–f).

While taking the hemispheric mean values, the regional features mainly from aerosol source regions can be missed out. So, the mean AOD and its trend over the aerosol source regions, for the regions India, eastern China, Europe, Africa and Middle-East, North-East America, and South America are given in Figure S4, and these regions were similar to the regions considered by Subba et al. (2020). All the models along with MMM and satellite data show a significant decreasing trend in North-East America and Europe (other than CESM2-WACCM and CESM2-WACCM-FV2); high mean AOD and a significant increasing trend depicted in India (other than CESM2-WACCM-FV2) and the eastern China region (other than CESM2-WACCM-FV2 and MISR); while considering the South America region, most of the models and MMM depicted insignificant trend and the satellite showed an insignificant decreasing pattern. In Africa and Middle-East region, CESM2-WACCM-FV2 showed high mean AOD values

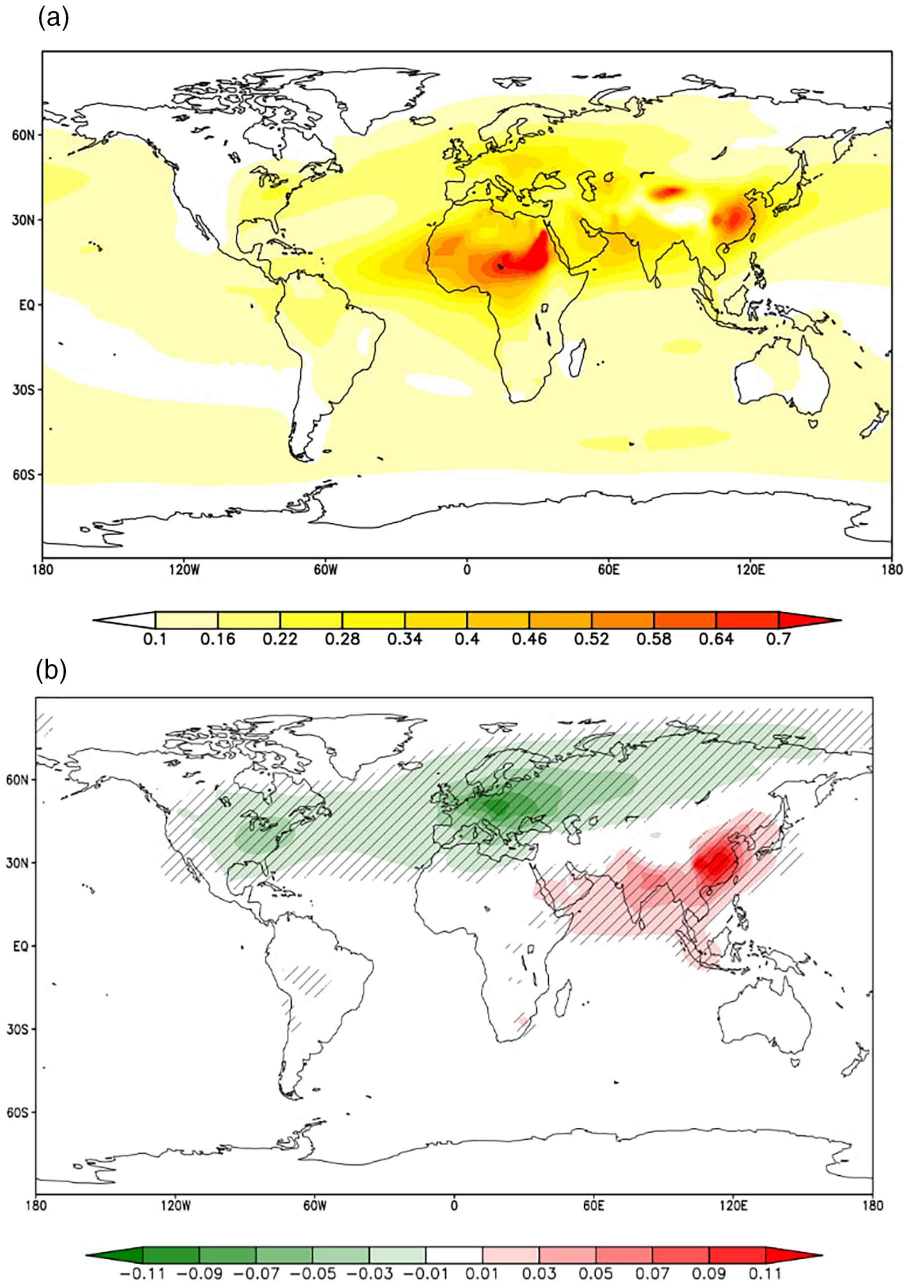

FIGURE 3 Spatial pattern of (a) Climatological mean annual AOD, (b) trend of annual AOD (in per decade scale) at 550 nm for the period 1971–2014 obtained from the MMM8. Here the hatched portion in (b) represents the statistical significance at a 0.05 level [Colour figure can be viewed at wileyonlinelibrary.com]

(∼0.7); while the AWI-ESM-1-1-LR, BCC-ESM-1-2, MPI-ESM-1-2-HR, MPI-ESM-1-2-LR and both the MMM showed significant positive trend and the satellite data also showed insignificant positive trend. The models AWI-ESM-1-1-LR, BCC-ESM-1-2, MPI-ESM-1-2-HR, and MPI-ESM-1-2-LR utilize prescribed aerosol schemes rather than incorporating interactive aerosol components. This results in some similarities between these models, irrespective of the higher or lower resolution of the models (Figures S1 and S2). In contrast, models such as CESM2-WACCM (MASINGAR mk2r4), CESM2-WACCM-FV2 (MASINGAR mk2r4), MPI-ESM-1-2-HAM (HAM2.0), and MRI-ESM-2-0 (MAM4) feature their unique interactive aerosol components, as indicated in Table 1 references. These components contribute to the generation of distinct aerosol patterns based on their respective features (Figures S1 and S2). While all these models may share similar emission inputs for aerosols and aerosol precursors, their diverse aerosol loadings in the atmosphere lead to the observed distinctions among them.

The decreasing trends in AOD as shown in Figure 2 were also detected in CMIP5 under representative concentration pathway (RCP4.5) future scenarios, which were reported to be due to the increased control of emissions (Rotstayn et al., 2013). The trends of AOD obtained from CMIP5, CMIP6, satellites, and reanalysis datasets showed that the multimodel ensembles were able to match the values obtained from satellites, but the individual models could not (Vogel et al., 2022). For obtaining the MMM, Vogel et al. (2022) used the AOD data from 21 CMIP6 GCMs over the region of 60°S–60°N and found that the average value of AOD is 0.16 for the period 1998–2014. In the present study, we have considered the six models (AWI–ESM-1-1-LR, BCC–ESM1, CESM2–WACCM, MRI-ESM 2-0, CESM–FV2 and MPI–ESM–HAM) among the 21 models chosen by Vogel et al. (2022) and the average AOD obtained from these six models for the region of 60°S–60°N are approximately 0.2 (land), 0.14 (ocean) and 0.16 (combined) for the period 1998–2014. It is also reported that uncertainties and differences among the models in simulating the AOD are mainly due to the uncertainties in the emission data sets (Vogel et al., 2022). It is reported that the mean AOD is higher in the Northern Hemisphere compared to the Southern Hemisphere and in the NH, the region covered between the equator and 40° tropical latitudes has more burden of aerosols (Aas et al., 2019). It is also reported that the annual trends are mostly positive in the tropical latitudes (Aas et al., 2019) and a positive trend in tropical SH due to the increased amount of biomass burning that gets transported from Australia and southeastern Africa (Hsu et al., 2012). These results were analogous to our findings where the AOD of NH (0.2) in the present study, which is higher than the SH (AOD = 0.11).

The mean annual AOD and it's trends for the period 1971–2014 obtained from the MMM8 are shown in Figure 3. The spatial pattern of AOD over the land region during the study period showed higher values than the oceanic regions. The lower values of AOD over North America and Europe were also observed. The mean value of AOD over Northern Africa and Eastern Asian regions is as high as 0.7, whereas they are as low as 0.05 over some oceanic regions and parts of polar regions (Figure 3a). Significant positive trends in AOD over parts of South and Southeast Asia along with a steep trend (+0.014/year or +0.6 mean annual AOD shift in the entire study period) concentrated over India and China can be seen in Figure 3b, which are in the tropical regions of NH. These findings of the spatial pattern of trends are analogous to the trends obtained from the CERES (combined data sets of MODIS and ESM) where the aerosol optical thickness over land is found larger than the ocean (Obregón et al., 2021). The increasing trends of AOD (Figure 3a), particularly in eastern China, are reported to be due to the underestimation of the recent decline in anthropogenic aerosol trends by CMIP6 during the recent decades (Wang et al., 2021). The in situ measurements of aerosols indicate an increase in aerosols over the Indian region (Babu et al., 2013). Also, Subba et al. (2022) reported surface radiative forcing over different parts of India such as Indo Gangetic Plains (IGP) ($-49\ \mathrm{W{\cdot}m^{-2}}$), northeast India ($-45\ \mathrm{W{\cdot}m^{-2}}$) and the southern peninsular region ($-34\ \mathrm{W{\cdot}m^{-2}}$) was mainly due to the anthropogenic sulphates and carbonaceous aerosols for the study period 2011–2014. The negative significant trend was found in the entire Europe region (−0.011/year or −0.4 mean annual AOD shift in the entire study period), western Russia, and the eastern parts of North America. These negative trends over the United States and Europe are mainly due to the reduction in emissions (Pozzer et al., 2015) which was the result of the different policies followed to control emissions in recent decades (Obregón et al., 2020; Wild, 2010; Wild et al., 2005). This model simulated dipole trend pattern between NM and NT regions is backed by the satellite-derived and surface-based observations of aerosols (Wei et al., 2019; Yu et al., 2020). The increasing trends of AOD in our study (Figure 3a) over North Africa and the Middle East were also observed by Pozzer et al. (2015) with the simulations of the EMAC (ECHAM5/MESSy Atmospheric Chemistry) model but with the lesser values compared to the observations. These differences in the magnitude of trends over these regions are found to be due to the emission data without any variability of the source regions (Astitha et al., 2012) and lesser amounts of precipitation simulations in the models.

3.2 | Biases in AOD simulations relative to MODIS and MISR data

The percent bias of AOD in MMM8 with the AOD of MODIS and MISR are shown in Figure 4a,b. In both cases, the bias pattern seems to be the same but with different bias percentages. Numerous studies exist in reporting the trends of AOD from models and satellites (Cherian & Johannes, 2020; Gupta et al., 2022; Itahashi et al., 2021; Li et al., 2021; Misra et al., 2016; Pozzer et al., 2015), but a few studies reported the biases of models with respect to the satellite data (Gliß et al., 2021; Schutgens et al., 2020; Vogel et al., 2022). Understanding the spatial distribution of percentage bias provides information on model performance in different aerosol environments. A study by Sockol et al. (2017) reported that the GCMs of CMIP5 (CAM5, GFDL, MIROC, MRI-ESM1-M) underestimated the AOD of MODIS by 15% globally. However, the bias varies regionally as CAM5 overestimated the AOD along the equator and over large portions of the Southern Hemisphere. It is also observed that the bias between models and satellites can vary seasonally. Studies on regional comparison of CMIP5 models with MODIS and MISR AOD over India from 2000 to 2005 found that MMM overestimated the MISR while it

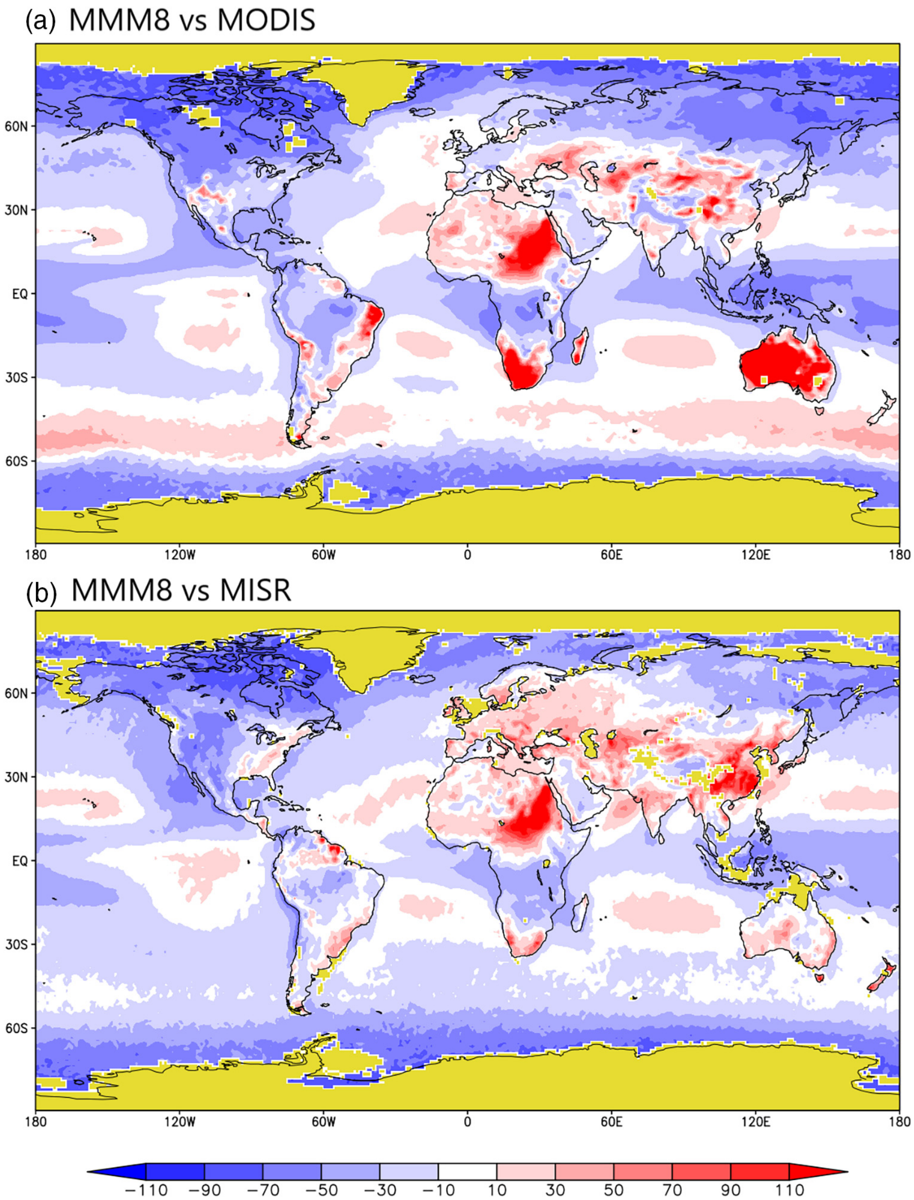

FIGURE 4 Spatial pattern of percent bias (%) of mean annual AOD at 550 nm obtained from MMM8 against the AOD of (a) MODIS and (b) MISR for the period of 2001–2014. Missing data points are represented in yellow [Colour figure can be viewed at wileyonlinelibrary.com]

underestimated MODIS AOD (Misra et al., 2016). A comparison of MODIS AOD with the CMIP6 ensemble of 15 GCMs for the period 2000–2014 showed that the model underestimated the satellite data over different parts of China (Ali et al., 2022). In the present analysis, we have got a model bias of −10.6% with MODIS and −13.8% with MISR on the global scale, respectively, which means that the MMM8 underestimated the AOD in most of the regions when compared against the satellite AOD. It is worth noting that the bias of MMM8 with MODIS and MISR is less in the Tropics (about −6% and −8%) when averaged over the entire region. The bias in the NM region with MODIS and MISR is −15.2% and −10.1% while, it is +6.4% and −14.7% over the SM region, respectively.

The mean bias is low over the Tropics because it is the average of large positive and large negative biases. China and India are the regions with more aerosol burden in the tropical region and this will be masked when the bias is averaged over the entire Tropics. Hence, we have also estimated the Absolute Percent Bias (APB) to delineate the changes from the reference datasets (Table 2). It is understood that the global APB of MMM8 with MODIS and MISR are 28.1% and 24.1%, respectively. The APB is highest over NP (56.4 and 48.1%) followed by SP (48.6 and 57.0%) with MODIS and MISR, respectively. The APB for the ST is 33.2/18.4% and NT is 24.5/22.6% with MODIS/MISR. Upon examination of various regions, it was observed that all regions exhibited an absolute percent bias (APB) ranging from 17% to 52%. When comparing these regions to MODIS/MISR data, the Europe region displayed the lowest APB, standing at 17.3/27.4, while eastern China exhibited the highest APB, reaching 26.8/51.8. The remaining regions had APB values as follows: India,

TABLE 2 Percentage of bias in MMM8 in different regions when compared against satellites (MODIS and MISR) for the mean 2010 to 2014 period

	MMM8 vs. MODIS (%)		MMM8 vs. MISR (%)	
Regions	Abs. magnitude	Total sum	Abs. magnitude	Total sum
India	22.8	−8.0	22.1	3.9
Eastern China	26.8	14.9	51.8	49.3
Europe	17.3	6.5	27.4	23.0
Africa and Middle East	26.7	4.1	22.0	−0.1
North-East America	26.2	−28.0	22.2	−16.8
South America	23.0	−9.7	18.8	−11.2
Globe	28.1	−10.6	24.1	−13.8
NH	28.7	−17.4	27.1	−10.6
SH	27.5	−3.5	21.0	−17.0
NP	56.4	−56.4	48.1	−46.4
NM	25.6	−15.2	27.1	−10.1
NT	24.5	−10.0	22.6	−3.4
ST	33.2	−4.0	18.4	−12.6
SM	15.3	6.4	17.0	−14.7
SP	48.6	−48.6	57.0	−57.0

22.8/22.1; Africa and Middle East, 26.7/22.0; North-East America, 26.2/22.2; and South America, 23/18.8. It is to be mentioned here that the study of Ali et al. (2022) reported the APB of AOD over China between the CMIP6 and MERRA-2 as 23%. The discrepancies in CMIP6 models with the satellites in depicting the actual aerosol concentration have been reported by Zhao et al. (2022), Wang et al. (2021), and Li et al. (2021). The comparison of dust optical depth (DOD) from CMIP6 with ModIs Dust AeroSol (MIDAS) data sets for the period 2005–2014 found that the CMIP6 overestimated the DOD by about 1.2–1.7 times when compared against the satellites over northern China and North America (Zhao et al., 2022). In the present work, the MMM8 underestimated and overestimated the AOD up to −40% and +80% in the IGP region in India and central China, respectively, in comparison with MODIS. Further, the MMM8 overestimated the AOD up to +105% in eastern China (EC) and central China (CC) in comparison with MISR. The CMIP6 GCMs showed a positive trend of AOD during 2006–2014 in EC and CC, contrarily the observations depict a decreasing trend of aerosols in the same period and this might be the reason for the high bias over the regions of China (Wang et al., 2021). Wang et al. (2021) have also compared the Indian and EC AOD from CMIP6 of 2006–2014 with their own GCM AOD, simulated with more reliable and updated emission datasets from Peking University, and stated that this discrepancy is due to the adaptation of the apparently flawed emission inventory—Community Emissions Data System (CEDS) by CMIP6 GCMs. This negative trend in EC and CC is attributable to the mitigation measures adopted by China from the beginning of the 21st century by decreasing its SO2 emissions by ~70% from 2006 to 2014 (Li et al., 2017).

Australia and the South African region have shown a complete contrast of bias with MODIS and MISR. When compared against the MODIS, MMM8 overestimated the AOD over Australia and South Africa (more than 100%) while MISR comparison did not show such high biases in the aforementioned regions. South Africa and Australia (Oceania) present low mean AOD values and the occasional high aerosol loading events are due to the wildfire smoke (Mukkavilli et al., 2019). Gui et al. (2021) evaluated MISR's Level-3 AOD products using global ground-based and regional aerosol data, finding good agreement but noting MISR's tendency to overestimate low AOD and underestimate high AOD values, mainly due to coarse-mode overestimation and fine-mode underestimation. Shaylor et al. (2022) reported MODIS DB algorithm depicting underestimation of AOD up to 50% compared to Multi-Angle Implementation of Atmospheric Correction (MAIAC) algorithms in the Australia region. Furthermore, Chen et al. (2022) reported that MODIS underestimated the AOD in the Australia (Oceania) region (~−0.02 AOD) during the period 2012–2019. This variation is primarily linked to sensor calibration in capturing the small variations in the low aerosol

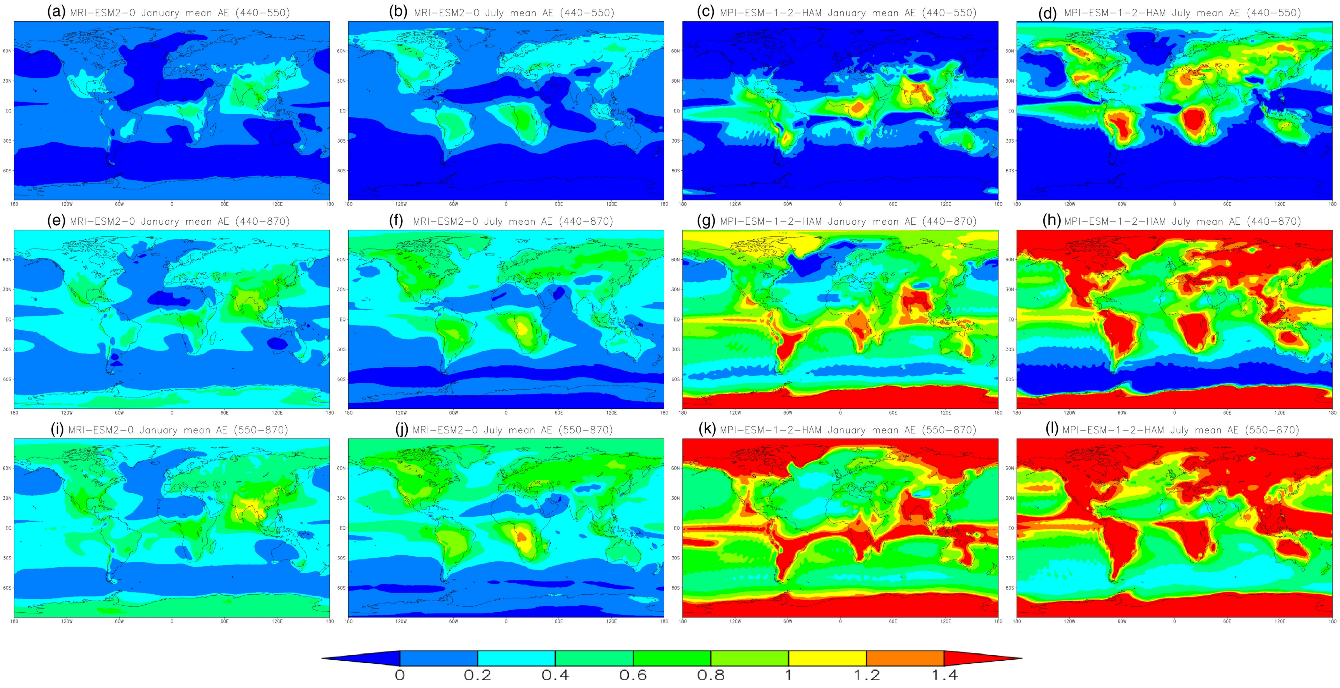

FIGURE 5 Spatial pattern of Angstrom exponent (α) obtained from AOD at wavelength combination of (a) 440–550 nm for January (MRI-ESM2-0), (b) 440–550 nm for July (MRI-ESM2-0), (c) 440–550 nm for January (MPI-ESM-1-2-HAM 0), (d) 440–550 nm for July (MPI-ESM-1-2-HAM), (e) 440–870 nm for January (MRI-ESM2-0), (f) 440–870 nm for July (MRI-ESM2-0), (g) 440–870 nm for January (MPI-ESM-1-2-HAM 0), (h) 440–870 nm for July (MPI-ESM-1-2-HAM, (i) 550–870 nm for January (MRI-ESM2-0), (j) 550–870 nm for July (MRI-ESM2-0), (k) 550–870 nm for January (MPI-ESM-1-2-HAM-0), (l) 550–870 nm for July (MPI-ESM-1-2-HAM) for the 1971–2014 period [Colour figure can be viewed at wileyonlinelibrary.com]

loading atmospheres (Sayer et al., 2019). It is reported that biomass-burning aerosols show more absorbing values in the recent global climate models (Brown et al., 2021). The contribution of biomass-burning aerosols to the global biomass burning by Africa is ~52% and Australia is ~7% (van der Werf et al., 2010). Also, the aircraft measurements on biomass burning aerosols over Africa showed large discrepancies when compared with the models. These might contribute to the higher amounts of bias in the models with the satellites (MODIS and MISR) over Australia and African regions. It is also worth noting that the trends obtained from the MODIS and MISR showed different signs over Northern Hemispheric high-latitude oceans and Southern Hemisphere oceans during the period 2000–2019 (Quaas et al., 2022). Overall, the MMM8 might underestimate or overestimate the AOD relative to MODIS/MISR over different regions, but the MODIS and MISR themselves overestimate or underestimate the AOD at different regions relative to other satellites and ground-based measurements (Chen et al., 2022; Levy et al., 2018; Schutgens et al., 2020). So, MODIS/MISR itself can be responsible for part of the discrepancies observed in the present study.

3.3 | Global distribution of model-derived AE

The spatial pattern of AE obtained from the combination of 440–550 nm, 440–870 nm, and 550–870 nm for the January and July months, from the perturbed initial condition ensemble of models MRI-ESM2-0 and MPI-ESM-1-2-HAM to the period 1971–2014 are shown in Figure 5. Also, the derivative of the AE from the two models for the January and July months on a global scale are shown in Figure 6. The selection of the different wavelength-AODs to estimate the AE will help to understand the various particle sizes in the atmosphere. The spatial distribution of AE and the derivative of AE infer how the climate models show the size distribution of regional aerosols across the globe. From Figures 5 and 6, it can be observed that the AE has lower values over the ocean regions compared to the land region, which represents the dominance of coarse mode particles over oceanic regions. However, the values of AE varied when the combination of different wavelengths was considered. The AE estimated from 550 and 870 nm (Figure 5i–l) have shown higher value distribution over the oceanic regions when compared with the other combinations such as 440–550 nm (Figure 5a–d) and 440–870 nm (Figure 5e–h).

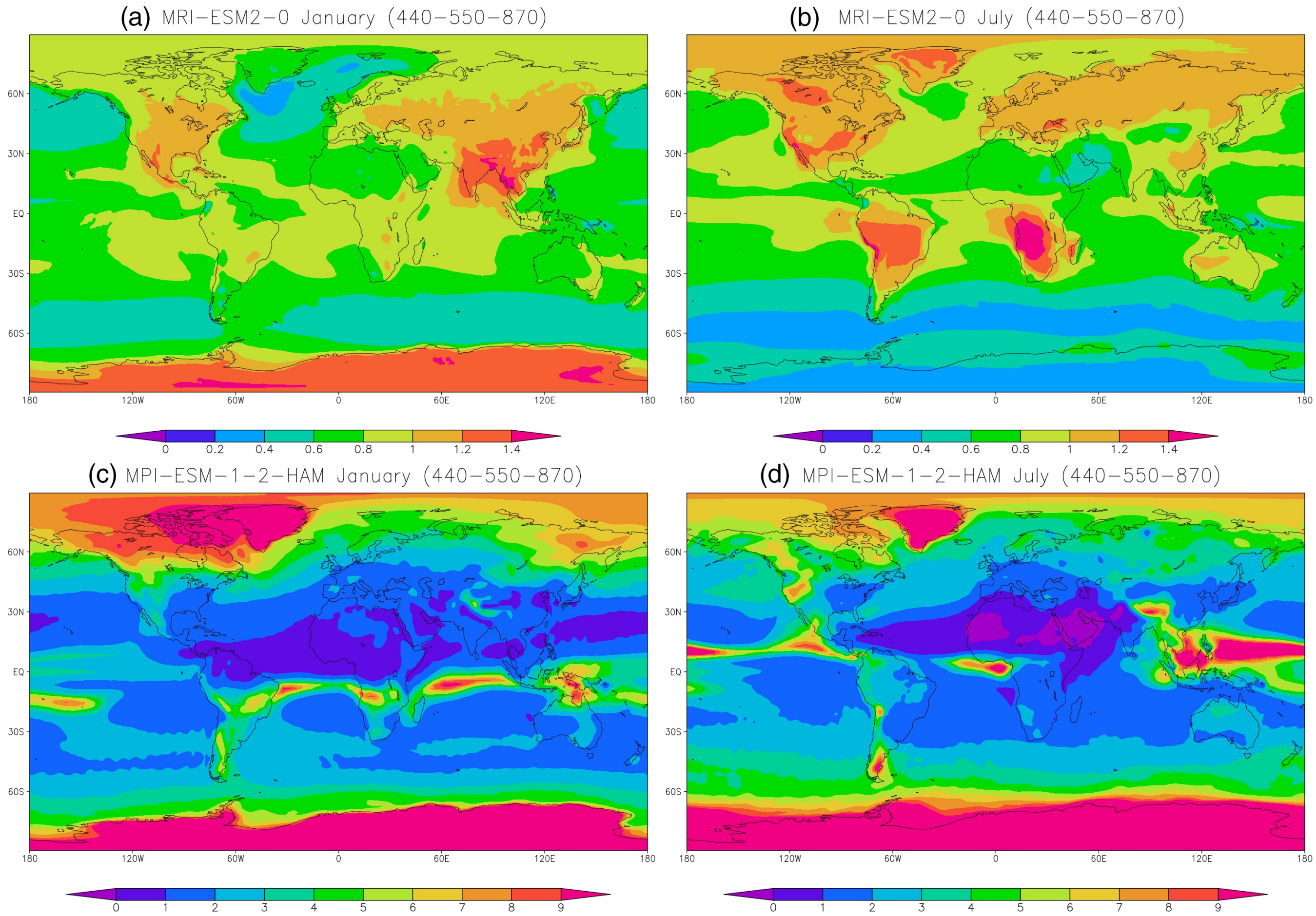

FIGURE 6 Spatial pattern of the derivative of Angstrom exponent (α') at wavelength combination of 440, 550, and 870 nm for (a) January month (MRI-ESM2-0), (b) July month (MRI-ESM2-0), (c) January month (MPI-ESM-1-2-HAM-0), (d) July month (MPI-ESM-1-2-HAM) for the 1971–2014 period [Colour figure can be viewed at wileyonlinelibrary.com]

Similar features are found with the AE values estimated from the MPI-ESM-1-2-HAM model too. The AE values are maximum in January over Southern Asia, Southern Africa, and South America regions of the Tropics when compared to other land regions (Figures 5 and 6). The AE pattern obtained from MPI-ESM-1-2-HAM over land showed the dominance of fine-mode aerosols over many regions and the estimate of AE is higher in most of the regions compared to the AE obtained from the MRI-ESM2-0 model. The AE pattern estimated from the 440–550 nm AOD showed the dominance of coarse-mode aerosols over the polar regions. While the AE pattern estimated from the combination of 440–870 nm and 550–870 nm of AOD showed the dominance of fine-mode aerosols over the southern polar region and both the polar regions, respectively. The presence of the fine-mode particles is found over some of the oceanic regions along with regions of North America, Russia, etc. when estimated from the combination of 550–870 nm AOD. AE pattern estimated for July month from the two models shows the dominance of coarse and fine-mode particles over ocean and land, respectively (Figure 5b,d,f,h,j,l). The values of AE increased during July month when compared to January month with more spatial distribution. The pattern of the first derivative of AE obtained from the MRI-ESM2-0 for the January and July months showed the presence of fine-mode particles in the January month over the southern polar region and the presence of coarser mode particles over the same region during the July month (Figure 6a,b). However, the model MPI-ESM-1-2-HAM showed the pattern of the first derivative of AE of fine-mode particles over the southern polar region (Figure 6c,d).

The overall analysis shows a disagreement between the two models in depicting the AE pattern over the southern polar region when the combination of 550–870 nm AOD has been considered. Also, the disagreement is conspicuous with the pattern of the first derivative of AE obtained for July month over the southern polar region. Another point that is worth noting is the

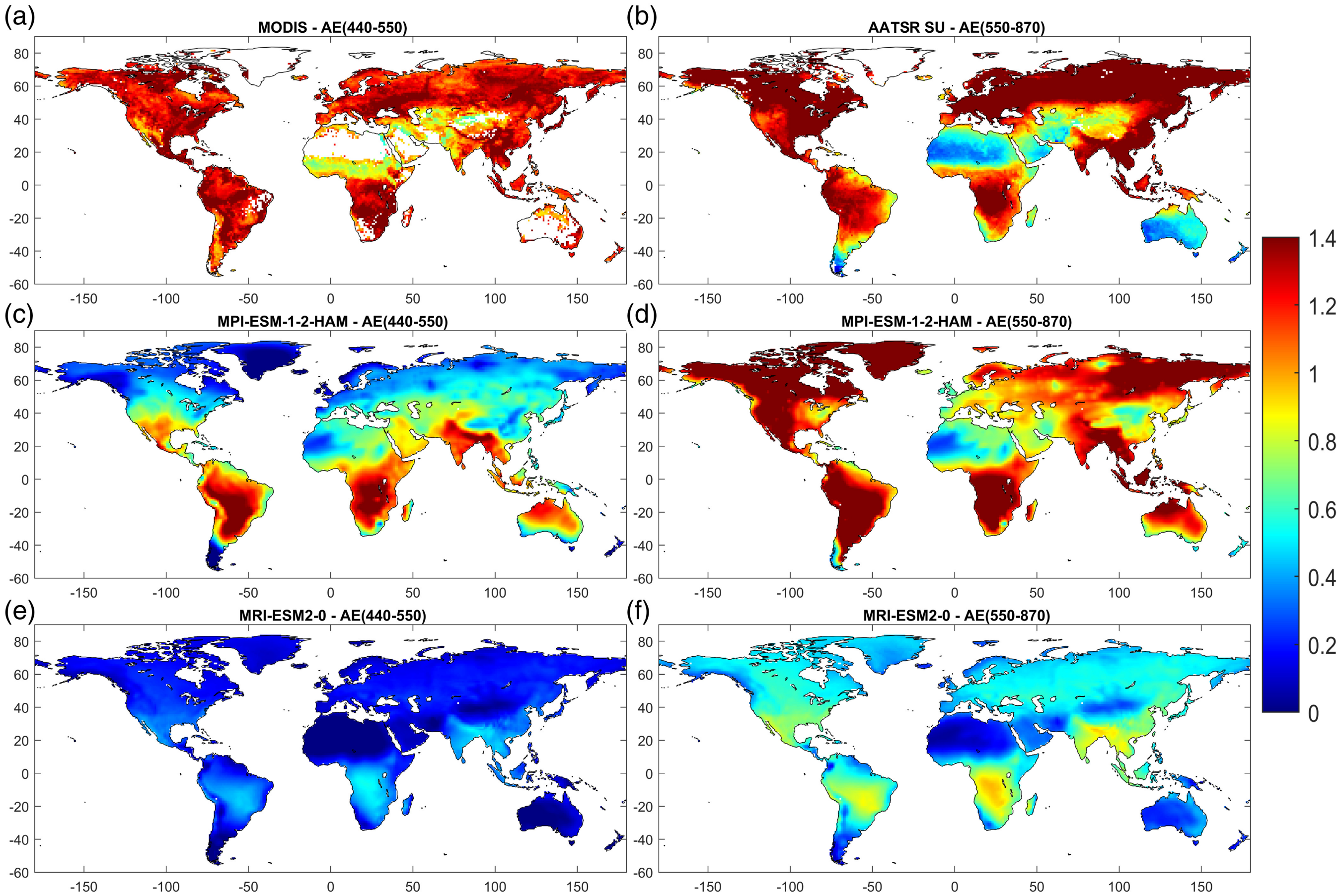

FIGURE 7 Spatial pattern of mean Angstrom exponent (α') (a) MODIS (440–550 AE), (b) AATSR SU (550–870 AE), (c) MPI-ESM-1-2-HAM (440–550 AE), (d) MPI-ESM-1-2-HAM (550–870 AE), (e) MRI-ESM2-0 (440–550 AE) and (f) MRI-ESM2-0 (550–870 AE) for the 2002–2012 period [Colour figure can be viewed at wileyonlinelibrary.com]

AE pattern could show the dominance of fine- and coarse-mode aerosols during January and July, respectively, obtained from both models in the Indian region, particularly matching with the seasonality of the Indian subcontinent. The January/July months are winter/monsoon months over India characterized by the dominance of continental/coarse mode aerosols. Surface wind climatology figures obtained from the NCEP reanalysis datasets during 1971–2014 for the January and July months provide a clue for the transport of the aerosols to different regions (Figure S5a,b). From Figure S5a, it can be seen that India has the dominance of north-westerlies in January while it is mostly south-westerlies during the month of July (Figure S5b). North-westerlies from the continental region depict the transport of anthropogenic aerosols that are mostly fine mode (Yan et al., 2021) during winter months over India. Southwesterlies during July represent the transport of the oceanic aerosols that are mostly coarse mode (Fitzgerald, 1991) over India.

A few studies reported the size distribution of aerosols using the AOD simulations across different regions of the globe (Kaiser et al., 2012; Liu et al., 2006; Mortier et al., 2020; Tegen et al., 2019). Studies by Mortier et al. (2020) reported that the CMIP6 models were able to well capture the particulate matter, sulphates, and the trends of AE in major portions of the globe. The key findings of Tegen et al. (2019) on the validation of AE simulated from the ECHAM6.3-HAM2.3 model found that the AE patterns estimated from 460 and 540 nm AOD have shown the presence of fine-mode particles over the regions of North Africa, South America, and ocean. Simulations using the GFAS (Global Fire Assimilation System) version 1.0 emission dataset also indicated the dominance of fine-mode aerosols in those regions (Kaiser et al., 2012). The discrepancies between model-simulated and observational AE are reported to be due to mainly the aerosol schemes assumed in the models for simulating the AOD. Liu et al. (2006) reported that the global distribution of AE obtained from the general circulation models shows a clear bias with the in situ measurements, which is due to the higher variability of AOD obtained from the models.

Although the models successfully capture spatial and seasonal variations that align with global circulation patterns, it is essential to validate the Angstrom exponent (AE) values generated by these models against satellite retrievals. In this section, we present the validation and comparison of simulated AE values derived from the MPI-ESM-1-2-HAM and MRI-ESM2-0 models' PPE with data from MODIS and AATSR SU. Figure 7 illustrates the spatial patterns of mean AE, as follows: (a) MODIS (440–550 AE), (b) AATSR SU (550–870 AE), (c) MPI-ESM-1-2-HAM (440–550 AE), (d) MPI-ESM-1-2-HAM (550–870 AE), (e) MRI-ESM2-0 (440–550 AE) and (f) MRI-ESM2-0 (550–870 AE). Since satellite retrievals of AOD data only have data over land for different spectral bands, our analysis specifically focuses on land-based AE features. A notable observation is that the MRI-ESM2-0 model consistently underestimates AE compared to both satellite observations (Figures 7 and S6). Specifically, MRI-ESM2-0 globally underestimates AE by 84% concerning MODIS and 54% concerning AATSR SU. In contrast, the MPI-ESM-1-2-HAM model exhibits differing behaviour, globally underestimating AE by 43% in the 440–550 AE range against MODIS but overestimating AE by 32% compared to AATSR SU. On a regional scale, MPI-ESM-1-2-HAM demonstrates fewer biases in AE, particularly in regions such as India (APB, 21.1%/17.3%), Africa, and the Middle East (ABP, 21.8%/24.8%), when compared to MODIS/AATSR SU AE values. Irrespective of the region, MRI-ESM-0 consistently underestimates AE values by 40%–80%. This consistent underestimation in the models suggests that they may either simulate larger aerosol particles than what is observed or underestimate the fraction of fine-mode aerosols. While the MPI-ESM-1-2-HAM model may demonstrate improved performance in certain regions, a comparison with AATSR-SU data indicates that the models tend to underestimate AE in Europe and North-East America. It is worth noting that the significant overestimation of AE over Australia and South America, compared to AATSR data, may be attributed to retrieval errors in the satellite product (Glïß et al., 2021).

4 | CONCLUSIONS

The increasing recognition of the importance of atmospheric aerosols has drawn the scientific community to use large-scale aerosol datasets for different weather and climate applications. The model simulations of AOD are abundant for the user community. However, the utilization of these datasets needs careful attention due to their uncertainties.

Hence, the evaluation of AOD datasets obtained from the models is essential for reliable climate predictions. In the present study, we have analysed the AOD of eight GCMs of CMIP6 to infer their behaviour in terms of magnitude, trends, bias, as well as size distribution with respect to satellite data observations. Based on our analysis we conclude the following:

1. The global AOD trend is insignificantly declining for the period 1971–2014. Significant positive trends were observed over the northern tropical region. The AOD over the Northern Hemisphere is high (0.2) due to its land–ocean contrast compared to the Southern Hemisphere for which the mean AOD is (0.11).
2. The MMM8 has overestimated the MODIS AOD over North Africa, India, China, and Australia while this overestimation is confined to North Africa and eastern China when compared against MISR AOD. The APB between MMM8 and MODIS/MISR is 28.1% and 24.1% over the globe.
3. During the winter and summer seasons, the spatial distribution of AE revealed a dominance of fine- and coarse-mode particles, respectively, which replicated the seasonality of aerosols. The AE obtained from the perturbed initial condition ensemble of MPI-ESM-1-2-HAM has shown a better agreement with the AE of AATSR SU (550–870 nm) than MODIS' AE (440–550 nm). In contrast, MRI-ESM2-0 consistently underestimated AE across various regions and wavelength ranges, indicating a prevalence of larger aerosol particles in the model's depiction of the aerosol size distribution compared to satellite observations.

Though there are studies for evaluating the global AOD simulations with the satellites and in situ measurements, the present study deals with the CMIP6 simulations of AOD in comparison with MODIS and MISR. This may help in understanding the performance of CMIP6 models in terms of trends, spatiotemporal distribution, and their biases with the satellites regionally and globally as well. In this way, the results of the study would provide additional insights into the knowledge of the global distribution of AOD and their size distribution.

AUTHOR CONTRIBUTIONS

J. Bharath: Software; data curation; investigation; formal analysis; methodology; writing – original draft. **T. V. Lakshmi Kumar:** Conceptualization; methodology; investigation; validation; supervision; writing – review and editing; writing – original draft. **Vanda Salgueiro:** Investigation; formal analysis; writing – review and editing; funding acquisition. **Maria João Costa:** Investigation; formal analysis; funding acquisition; project administration; writing – review and editing. **R. K. Mall:** Writing – review and editing; supervision.

ACKNOWLEDGEMENTS

We acknowledge the World Climate Research Program's Working Group on Coupled Modeling, which is responsible for the CMIP, and the GES-DISC for providing gridded AOD products of MODIS and MISR through their Giovanni website. The work was co-funded by National Portuguese funds through FCT-Fundação para a Ciência e Tecnologia, I.P. (projects UIDB/04683/2020 and UIDP/04683/2020). The authors are grateful to the anonymous reviewers for their critical comments that improved the manuscript significantly.

DATA AVAILABILITY STATEMENT

The dataset used in the present study are open source. Codes will be made available based on the reasonable request.

ORCID

Jaisankar Bharath https://orcid.org/0000-0002-0790-2045
Tumuluru Venkata Lakshmi Kumar https://orcid.org/0000-0002-6191-7969
Maria João Costa https://orcid.org/0000-0003-2981-2232
Rajesh Kumar Mall https://orcid.org/0000-0002-3118-096X

REFERENCES

Aas, W., Mortier, A., Bowersox, V., Cherian, R., Faluvegi, G., Fagerli, H. et al. (2019) Global and regional trends of atmospheric sulfur. *Scientific Reports*, 9(1), 953. Available from: https://doi.org/10.1038/s41598-018-37304-0

Ali, M.A., Bilal, M., Wang, Y., Qiu, Z., Nichol, J.E., de Leeuw, G. et al. (2022) Evaluation and comparison of CMIP6 models and MERRA-2 reanalysis AOD against satellite observations from 2000 to 2014 over China. *Geoscience Frontiers*, 13(2), 101325. Available from: https://doi.org/10.1016/j.gsf.2021.101325

Andreae, M.O., Jones, C.D. & Cox, P.M. (2005) Strong present-day aerosol cooling implies a hot future. *Nature*, 435(7046), 1187–1190. Available from: https://doi.org/10.1038/nature03671

Astitha, M., Lelieveld, J., Abdel Kader, M., Pozzer, A. & de Meij, A. (2012) Parameterization of dust emissions in the global atmospheric chemistry-climate model EMAC: impact of nudging and soil properties. *Atmospheric Chemistry and Physics*, 12, 11057–11083. Available from: https://doi.org/10.5194/acp-12-11057-2012

Babu, S.S., Manoj, M.R., Moorthy, K.K., Gogoi, M.M., Nair, V.S., Kompalli, S.K. et al. (2013) Trends in aerosol optical depth over Indian region: potential causes and impact indicators. *Journal of Geophysical Research: Atmospheres*, 118(20), 11794–11806. Available from: https://doi.org/10.1002/2013jd020507

Boé, J. (2016) Modulation of the summer hydrological cycle evolution over Western Europe by anthropogenic aerosols and soil–atmosphere interactions. *Geophysical Research Letters*, 43(14), 7678–7685. Available from: https://doi.org/10.1002/2016gl069394

Brown, H., Liu, X., Pokhrel, R., Murphy, S., Lu, Z., Saleh, R. et al. (2021) Biomass burning aerosols in most climate models are too absorbing. *Nature Communications*, 12, 277. Available from: https://doi.org/10.1038/s41467-020-20482-9

Chen, Q.-X., Xin-Lei Han, Y.G., Yuan, Y., Jiang, J.H., Yang, X.-B., Liou, K.-N. et al. (2022) Evaluation of MODIS, MISR, and VIIRS daily level-3 aerosol optical depth products over land. *Atmospheric Research*, 265, 105810. Available from: https://doi.org/10.1016/j.atmosres.2021.105810

Cherian, R. & Johannes, Q. (2020) Trends in AOD, clouds, and cloud radiative effects in satellite data and CMIP5 and CMIP6 model simulations over aerosol source regions. *Geophysical Research Letters*, 47(9), e2020GL087132. Available from: https://doi.org/10.1029/2020gl087132

Christensen, M.W., Jones, W.K. & Stier, P. (2020) Aerosols enhance cloud lifetime and brightness along the stratus-to-cumulus transition. *PNAS*, 117(30), 17591–17598.

Chung, E.-S. & Soden, B.J. (2017) Hemispheric climate shifts driven by anthropogenic aerosol–cloud interactions. *Nature Geoscience*, 10(8), 566–571. Available from: https://doi.org/10.1038/ngeo2988

Deep, A., Pandey, C.P., Nandan, H., Singh, N., Yadav, G., Joshi, P.C. et al. (2021) Aerosols optical depth and Ångström exponent over different regions in Garhwal Himalaya, India. *Environmental Monitoring and Assessment*, 193, 324. Available from: https://doi.org/10.1007/s10661-021-09048-4

Eck, T.F., Holben, B.N., Ward, D.E., Dubovik, O., Reid, J.S., Smirnov, A. et al. (2001) Characterization of the optical properties of biomass burning aerosols in Zambia during the 1997 ZIBBEE field campaign. *Journal of Geophysical Research*, 106(D4), 3425–3448. Available from: https://doi.org/10.1029/2000jd900555

Ekman, A.M.L. (2014) Do sophisticated parameterizations of aerosol–cloud interactions in CMIP5 models improve the representation of recent observed temperature trends? *Journal of Geophysical Research*, 119(2), 817–832. Available from: https://doi.org/10.1002/2013jd020511

Eyring, V., Bony, S., Meehl, G.A., Senior, C.A., Stevens, B., Stouffer, R.J. et al. (2016) Overview of the Coupled Model Intercomparison Project phase 6 (CMIP6) experimental design and organization. *Geoscientific Model Development*, 9(5), 1937–1958. Available from: https://doi.org/10.5194/gmd-9-1937-2016

Fitzgerald, J.W. (1991) Marine aerosols: a review. *Atmospheric Environment. Part A. General Topics*, 25(3), 533–545.

Frey, L., Bender, F.A.M. & Svensson, G. (2017) Cloud albedo changes in response to anthropogenic sulfate and non-sulfate aerosol forcings in CMIP5 models. *Atmospheric Chemistry and Physics*, 17(14), 9145–9162.

Gliß, J., Mortier, A., Schulz, M., Andrews, E., Balkanski, Y., Bauer, S.E. et al. (2021) AeroCom phase III multi-model evaluation of the aerosol life cycle and optical properties using ground-and space-based remote sensing as well as surface in situ observations. *Atmospheric Chemistry and Physics*, 21(1), 87–128. Available from: https://doi.org/10.5194/acp-21-87-2021

Gui, K., Che, H., Wang, Y., Xia, X., Holben, B.N., Goloub, P. et al. (2021) A global-scale analysis of the MISR Level-3 aerosol optical depth (AOD) product: comparison with multi-platform AOD data sources. *Atmospheric Pollution Research*, 12(12), 101238. Available from: https://doi.org/10.1016/j.apr.2021.101238

Gupta, G., Venkat Ratnam, M., Madhavan, B.L. & Narayanamurthy, C.S. (2022) Long-term trends in aerosol optical depth obtained across the globe using multi-satellite measurements. *Atmospheric Environment*, 273, 118953. Available from: https://doi.org/10.1016/j.atmosenv.2022.118953

Hawkins, E. & Sutton, R. (2009) The potential to narrow uncertainty in regional climate predictions. *Bulletin of the American Meteorological Society*, 90(8), 1095–1108. Available from: https://doi.org/10.1175/2009bams2607.1

Hsu, N.C., Gautam, R., Sayer, A.M., Bettenhausen, C., Li, C., Jeong, M.J. et al. (2012) Global and regional trends of aerosol optical depth over land and ocean using SeaWiFS measurements from 1997 to 2010. *Atmospheric Chemistry and Physics*, 12(17), 8037–8053. Available from: https://doi.org/10.5194/acp-12-8037-2012

Hua, S., Liu, Y., Luo, R., Shao, T. & Zhu, Q. (2020) Inconsistent aerosol indirect effects on water clouds and ice clouds over the Tibetan Plateau. *International Journal of Climatology*, 40(8), 3832–3848. Available from: https://doi.org/10.1002/joc.6430

Itahashi, S., Sakurai, T., Shimadera, H., Araki, S. & Hayami, H. (2021) Long-term trends of satellite-based fine-mode aerosol optical depth over the Seto Inland Sea, Japan, over two decades (2001–2020). *Environmental Research Letters*, 16(6), 064062.

Jung, J., Souri, A.H., Wong, D.C., Lee, S., Jeon, W., Kim, J. et al. (2019) The impact of the direct effect of aerosols on meteorology and air quality using aerosol optical depth assimilation during the KORUS–AQ campaign. *Journal of Geophysical Research: Atmospheres*, 124(14), 8303–8319.

Kaiser, J.W., Heil, A., Andreae, M.O., Benedetti, A., Chubarova, N., Jones, L. et al. (2012) Biomass burning emissions estimated with a global fire assimilation system based on observed fire radiative power. *Biogeosciences*, 9(1), 527–554. Available from: https://doi.org/10.5194/bg-9-527-2012

Kahn, R.A., Gaitley, B.J., Garay, M.J., Diner, D.J., Eck, T.F., Smirnov, A. et al. (2010) Multiangle imaging SpectroRadiometer Global Aerosol Product assessment by comparison with the aerosol robotic network. *Journal of Geophysical Research*, 115(D23), D23209. Available from: https://doi.org/10.1029/2010jd014601

Kahn, R., Banerjee, P. & McDonald, D. (2001) Sensitivity of multiangle imaging to natural mixtures of aerosols over ocean. *Journal of Geophysical Research*, 106(D16), 18219–18238. Available from: https://doi.org/10.1029/2000jd900497

Kang, N., Raghavendra Kumar, K., Kang, H., Xingna, Y. & Yin, Y. (2016) Long-term (2002–2014) evolution and trend in Collection 5.1 Level-2 aerosol products derived from the MODIS and MISR sensors over the Chinese Yangtze River Delta. *Atmospheric Research*, 181, 29–43. Available from: https://doi.org/10.1016/j.atmosres.2016.06.008

Kaufman, Y.J., Tanré, D., Remer, L.A., Vermote, E.F., Chu, A. & Holben, B.N. (1997) Operational remote sensing of tropospheric aerosol over land from EOS Moderate Resolution Imaging Spectroradiometer. *Journal of Geophysical Research*, 102(D14), 17051–17067. Available from: https://doi.org/10.1029/96jd03988

Klimont, Z., Smith, S.J. & Cofala, J. (2013) The last decade of global anthropogenic sulfur dioxide: 2000–2011 emissions. *Environmental Research Letters*, 8, 014003. Available from: https://doi.org/10.1088/1748-9326/8/1/014003

Klimont, Z., Kupiainen, K., Heyes, C., Purohit, P., Cofala, J., Rafaj, P. et al. (2017) Global anthropogenic emissions of particulate matter including black carbon. *Atmospheric Chemistry and Physics*, 17(14), 8681–8723. Available from: https://doi.org/10.5194/acp-17-8681-2017

Knobelspiesse, K.D., Pietras, C., Fargion, G.S., Wang, M., Frouin, R., Miller, M.A. et al. (2004) Maritime aerosol optical thickness measured by handheld Sun photometers. *Remote Sensing of the Environment*, 93(1–2), 87–106. Available from: https://doi.org/10.1016/j.rse.2004.06.018

Lauer, A. & Hamilton, K. (2013) Simulating clouds with global climate models: a comparison of CMIP5 results with CMIP3 and satellite data. *Journal of Climate*, 26(11), 3823–3845. Available from: https://doi.org/10.1175/jcli-d-12-00451.1

Lelieveld, J., Barlas, C., Giannadaki, D. & Pozzer, A. (2013) Model calculated global, regional and megacity premature mortality due to air pollution. *Atmospheric Chemistry and Physics*, 13(14), 7023–7037. Available from: https://doi.org/10.5194/acp-13-7023-2013

Levy, R.C., Mattoo, S., Munchak, L.A., Remer, L.A., Sayer, A.M. & Hsu, N.C. (2013) The Collection 6 MODIS aerosol products over land and ocean. *Atmospheric Measurement Techniques*, 6, 2989–3034. Available from: https://doi.org/10.5194/amtd-6-159-2013

Levy, R.C., Mattoo, S., Sawyer, V., Shi, Y., Colarco, P.R., Lyapustin, A.I. et al. (2018) Exploring systematic offsets between aerosol products from the two MODIS sensors. *Atmospheric Measurement Techniques*, 11(7), 4073–4092. Available from: https://doi.org/10.5194/amt-11-4073-2018

Li, C., McLinden, C., Fioletov, V., Krotkov, N., Carn, S., Joiner, J. et al. (2017) India is overtaking China as the world's largest emitter of anthropogenic sulfur dioxide. *Scientific Reports*, 7(1), 14304. Available from: https://doi.org/10.1038/s41598-017-14639-8

Li, X., Liu, Y., Wang, M., Jiang, Y. & Dong, X. (2021) Assessment of the Coupled Model Intercomparison Project phase 6 (CMIP6) model performance in simulating the spatial-temporal variation of aerosol optical depth over eastern Central China. *Atmospheric Research*, 261, 105747. Available from: https://doi.org/10.1016/j.atmosres.2021.105747

Lin, L., Wang, Z., Yangyang, X., Qiang, F. & Dong, W. (2018) Larger sensitivity of precipitation extremes to aerosol than greenhouse gas forcing in CMIP5 models. *Journal of Geophysical Research*, 123, 8062–8073. Available from: https://doi.org/10.1029/2018jd028821

Liu, L., Lacis, A.A., Carlson, B.E., Mishchenko, M.I. & Cairns, B. (2006) Assessing Goddard Institute for Space Studies ModelE aerosol climatology using satellite and ground-based measurements: a comparison study. *Journal of Geophysical Research*, 111, D20212. Available from: https://doi.org/10.1029/2006JD007334

Luo, R., Liu, Y., Zhu, Q., Tang, Y. & Shao, T. (2021) Effects of aerosols on cloud and precipitation in East-Asian drylands. *International Journal of Climatology*, 41(9), 4603–4618. Available from: https://doi.org/10.1002/joc.7089

Misra, A., Kanawade, V.P. & Tripathi, S.N. (2016) Quantitative assessment of AOD from 17 CMIP5 models based on satellite-derived AOD over India. *Annales Geophysicae*, 34(8), 657–671. Available from: https://doi.org/10.5194/angeo-34-657-2016

Monerie, P.-A., Wilcox, L.J. & Turner, A.G. (2022) Effects of anthropogenic aerosol and greenhouse gas emissions on Northern Hemisphere monsoon precipitation: mechanisms and uncertainty. *Journal of Climate*, 35(8), 2305–2326. Available from: https://doi.org/10.1175/JCLI-D-21-0412.1

Mortier, A., Gliß, J., Schulz, M., Aas, W., Andrews, E., Bian, H. et al. (2020) Evaluation of climate model aerosol trends with ground-based observations over the last 2 decades—an AeroCom and CMIP6 analysis. *Atmospheric Chemistry and Physics*, 20(21), 13355–13378. Available from: https://doi.org/10.5194/acp-20-13355-2020

Mukkavilli, S.K., Prasad, A.A., Taylor, R.A., Huang, J., Mitchell, R.M., Troccoli, A. et al. (2019) Assessment of atmospheric aerosols from two reanalysis products over Australia. *Atmospheric Research*, 215, 149–164. Available from: https://doi.org/10.1016/j.atmosres.2018.08.026

Myhre, G., Samset, B.H., Schulz, M., Balkanski, Y., Bauer, S., Berntsen, T.K. et al. (2013) Radiative forcing of the direct aerosol effect from AeroCom phase II simulations. *Atmospheric Chemistry and Physics*, 13(4), 1853–1877. Available from: https://doi.org/10.5194/acp-13-1853-2013

Myhre, G., Aas, W., Cherian, R., Collins, W., Faluvegi, G., Flanner, M. et al. (2017) Multi-model simulations of aerosol and ozone radiative forcing due to anthropogenic emission changes during the period 1990–2015. *Atmospheric Chemistry and Physics*, 17(4), 2709–2720. Available from: https://doi.org/10.5194/acp-17-2709-2017

Neal, R., Robbins, J., Dankers, R., Mitra, A., Jayakumar, A., Rajagopal, E.N. et al. (2020) Deriving optimal weather pattern definitions for the representation of precipitation variability over India. *International Journal of Climatology*, 40(1), 342–360.

Obregón, M.A., Costa, M.J., Silva, A.M. & Serrano, A. (2020) Spatial and temporal variation of aerosol and water vapour effects on solar radiation in the Mediterranean Basin during the last two decades. *Remote Sensing*, 12, 1316. Available from: https://doi.org/10.3390/rs12081316

Obregón, M.Á., Serrano, A., Costa, M.J. & Silva, A.M. (2021) Global spatial and temporal variation of the combined effect of aerosol and water vapour on solar radiation. *Remote Sensing*, 13, 708. Available from: https://doi.org/10.3390/rs13040708

Pozzer, A., De Meij, A., Yoon, J., Tost, H., Georgoulias, A.K. & Astitha, M. (2015) AOD trends during 2001–2010 from observations and model simulations. *Atmospheric Chemistry and Physics*, 15(10), 5521–5535. Available from: https://doi.org/10.5194/acp-15-5521-2015

Pu, B. & Ginoux, P. (2018) How reliable are CMIP5 models in simulating dust optical depth? *Atmospheric Chemistry and Physics*, 18(16), 12491–12510. Available from: https://doi.org/10.5194/acp-18-12491-2018

Qi, Y., Ge, J. & Huang, J. (2013) Spatial and temporal distribution of MODIS and MISR aerosol optical depth over northern China and comparison with AERONET. *Chinese Science Bulletin*, 58, 2497–2506. Available from: https://doi.org/10.1007/s11434-013-5678-5

Quaas, J., Jia, H., Smith, C., Albright, A.L., Aas, W., Bellouin, N. et al. (2022) Robust evidence for reversal of the trend in aerosol effective climate forcing. *Atmospheric Chemistry and Physics*, 22, 12221–12239. Available from: https://doi.org/10.5194/acp-22-12221-2022

Ramachandran, S., Rupakheti, M. & Cherian, R. (2022) Insights into recent aerosol trends over Asia from observations and CMIP6 simulations. *The Science of the Total Environment*, 807, 150756. Available from: https://doi.org/10.1016/j.scitotenv.2021.150756

Ramachandran, S., Rupakheti, M. & Lawrence, M.G. (2020) Aerosol-induced atmospheric heating rate decreases over South and East Asia as a result of changing content and composition. *Scientific Reports*, 10(1), 20091. Available from: https://doi.org/10.1038/s41598-020-76936-z

Ramanathan, V., Crutzen, P.J., Kiehl, J.T. & Rosenfeld, D. (2001) Aerosols, climate, and the hydrological cycle. *Science*, 294(5549), 2119–2124. Available from: https://doi.org/10.1126/science.1064034

Rotstayn, L.D., Collier, M.A., Chrastansky, A., Jeffrey, S.J. & Luo, J.-J. (2013) Projected effects of declining aerosols in RCP4.5: unmasking global warming? *Atmospheric Chemistry and Physics*, 13(21), 10883–10905. Available from: https://doi.org/10.5194/acp-13-10883-2013

Samset, B.H., Lund, M.T., Bollasina, M., Myhre, G. & Wilcox, L. (2019) Emerging Asian aerosol patterns. *Nature Geoscience*, 12(8), 582–584. Available from: https://doi.org/10.1038/s41561-019-0424-5

Sanap, S.D., Ayantika, D.C., Pandithurai, G. & Niranjan, K. (2014) Assessment of the aerosol distribution over Indian subcontinent in CMIP5 models. *Atmospheric Environment*, 87, 123–137. Available from: https://doi.org/10.1016/j.atmosenv.2014.01.017

Sanap, S.D., Pandithurai, G. & Manoj, M.G. (2015) On the response of Indian summer monsoon to aerosol forcing in CMIP5 model simulations. *Climate Dynamics*, 45, 2949–2961. Available from: https://doi.org/10.1007/s00382-015-2516-2

Sayer, A.M., Hsu, N.C., Lee, J., Kim, W.V. & Dutcher, S.T. (2019) Validation, stability, and consistency of MODIS Collection 6.1 and VIIRS version 1 Deep blue aerosol data over land. *Journal of Geophysical Research: Atmospheres*, 124, 4658–4688. Available from: https://doi.org/10.1029/2018JD029598

Schutgens, N., Sayer, A.M., Heckel, A., Hsu, C., Jethva, H., De Leeuw, G. et al. (2020) An AeroCom–AeroSat study: intercomparison of satellite AOD datasets for aerosol model evaluation. *Atmospheric Chemistry and Physics*, 20(21), 12431–12457. Available from: https://doi.org/10.5194/acp-20-12431-2020

Shaylor, M., Brindley, H. & Sellar, A. (2022) An evaluation of two decades of aerosol optical depth retrievals from MODIS over Australia. *Remote Sensing*, 14(11), 2664. Available from: https://doi.org/10.3390/rs14112664

Smith, S.J. & Bond, T.C. (2014) Two hundred fifty years of aerosols and climate: the end of the age of aerosols. *Atmospheric Chemistry and Physics*, 14(2), 537–549. Available from: https://doi.org/10.5194/acp-14-537-2014

Sobel, A.H., Camargo, S.J. & Previdi, M. (2019) Aerosol versus greenhouse gas effects on tropical cyclone potential intensity and the hydrologic cycle. *Journal of Climate*, 32(17), 5511–5527. Available from: https://doi.org/10.1175/JCLI-D-18-0357.1

Sockol, A., Griswold, S. & Jennifer, D. (2017) Intercomparison between CMIP5 model and MODIS satellite-retrieved data of aerosol optical depth, cloud fraction, and cloud-aerosol interactions. *Earth and Space Science*, 4, 485–505. Available from: https://doi.org/10.1002/2017EA000288

Stohl, A., Aamaas, B., Amann, M., Baker, L.H., Bellouin, N., Berntsen, T.K. et al. (2015) Evaluating the climate and air quality impacts of short-lived pollutants. *Atmospheric Chemistry and Physics*, 15(18), 10529–10566. Available from: https://doi.org/10.5194/acp-15-10529-2015

Subba, T., Gogoi, M.M., Pathak, B., Bhuyan, P.K. & Babu, S.S. (2020) Recent trend in the global distribution of aerosol direct radiative forcing from satellite measurements. *Atmospheric Science Letters*, 21(11), Portico. Available from: https://doi.org/10.1002/asl.975

Subba, T., Gogoi, M.M., Krishna Moorthy, K., Bhuyan, P.K., Pathak, B., Guha, A. et al. (2022) New estimates of aerosol radiative effects over India from surface and satellite observations. *Atmospheric Research*, 276, 106254. Available from: https://doi.org/10.1016/j.atmosres.2022.106254

Tebaldi, C. & Knutti, R. (2007) The use of the multi-model ensemble in probabilistic climate projections. *Philosophical Transactions of the Royal Society A: Mathematical, Physical and Engineering Sciences*, 365(1857), 2053–2075. Available from: https://doi.org/10.1098/rsta.2007.2076

Tegen, I., Neubauer, D., Ferrachat, S., Siegenthaler-Le Drian, C., Bey, I., Schutgens, N. et al. (2019) The global aerosol-climate model ECHAM6.3-HAM2.3—Part 1: aerosol evaluation. *Geoscientific Model Development*, 12(4), 1643–1677. Available from: https://doi.org/10.5194/gmd-12-1643-2019

van der Werf, G.R., Randerson, J.T., Giglio, L., Collatz, G.J., Mu, M., Kasibhatla, P.S. et al. (2010) Global fire emissions and the contribution of deforestation, savanna, forest, agricultural, and peat fires (1997–2009). *Atmospheric Chemistry and Physics*, 10, 11707–11735. Available from: https://doi.org/10.5194/acp-10-11707-2010

Vogel, A., Alessa, G., Scheele, R., Weber, L., Dubovik, O., North, P. et al. (2022) Uncertainty in aerosol optical depth from modern aerosol-climate models, reanalyses, and satellite products. *Journal of Geophysical Research: Atmospheres*, 127, e2021JD035483. Available from: https://doi.org/10.1029/2021JD035483

Wang, Z., Lin, L., Yangyang, X., Che, H., Zhang, X., Zhang, H. et al. (2021) Incorrect Asian aerosols affecting the attribution and projection of regional climate change in CMIP6 models. *npj Climate and Atmospheric Science*, 4(1), 1–8. Available from: https://doi.org/10.1038/s41612-020-00159-2

Wei, J., Peng, Y., Guo, J. & Sun, L. (2019) Performance of MODIS Collection 6.1 level 3 aerosol products in spatial-temporal variations over land. *Atmospheric Environment*, 206, 30–44. Available from: https://doi.org/10.1016/j.atmosenv.2019.03.001

Wild, M. (2010) Introduction to special section on global dimming and brightening. *Journal of Geophysical Research*, 115, D00D00. Available from: https://doi.org/10.1029/2009jd012841

Wild, M., Gilgen, H., Roesch, A., Ohmura, A., Long, C.N., Dutton, E.G. et al. (2005) From dimming to brightening: decadal changes in solar radiation at Earth's surface. *Science*, 308(5723), 847–850. Available from: https://doi.org/10.1126/science.1103215

Yan, X., Zang, Z., Liang, C., Luo, N., Ren, R., Cribb, M. et al. (2021) New global aerosol fine-mode fraction data over land derived from MODIS satellite retrievals. *Environmental Pollution*, 276, 707. Available from: https://doi.org/10.1016/j.envpol.2021.116707

Yu, H., Yang, Y., Wang, H., Tan, Q., Chin, M., Levy, R.C. et al. (2020) Interannual variability and trends of combustion aerosol and dust in major continental outflows revealed by MODIS retrievals and CAM5 simulations during 2003–2017. *Atmospheric Chemistry and Physics*, 20(1), 139–161. Available from: https://doi.org/10.5194/acp-20-139-2020

Zhao, A., Ryder, C.L. & Wilcox, L.J. (2022) How well do the CMIP6 models simulate dust aerosols? *Atmospheric Chemistry and Physics*, 22, 2095–2119. Available from: https://doi.org/10.5194/acp-22-2095-2022

Zhao, B., Jiang, J.H., Diner, D.J., Hui, S., Yu, G., Liou, K.-N. et al. (2018) Intra-annual variations of regional aerosol optical depth, vertical distribution, and particle types from multiple satellite and ground-based observational datasets. *Atmospheric Chemistry and Physics*, 18(15), 11247–11260. Available from: https://doi.org/10.5194/acp-18-11247-2018

SUPPORTING INFORMATION

Additional supporting information can be found online in the Supporting Information section at the end of this article.

How to cite this article: Bharath, J., Kumar, T. V. L., Salgueiro, V., Costa, M. J., & Mall, R. K. (2024). Aerosol characteristics in CMIP6 models' global simulations and their evaluation with the satellite measurements. *International Journal of Climatology*, *44*(1), 217–236. https://doi.org/10.1002/joc.8324